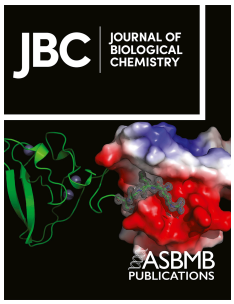

Dynamics of integrin α5β1, fibronectin, and their complex reveal sites of interaction and conformational change

Yang Su, Roxana E. Iacob, Jing Li, John R. Engen, Timothy A. Springer

PII: S0021-9258(22)00765-7

DOI: https://doi.org/10.1016/j.jbc.2022.102323

Reference: JBC 102323

To appear in: *Journal of Biological Chemistry*

Received Date: 10 February 2022

Revised Date: 26 July 2022

Accepted Date: 27 July 2022

Please cite this article as: Su Y, Iacob RE, Li J, Engen JR, Springer TA, Dynamics of integrin α5β1, fibronectin, and their complex reveal sites of interaction and conformational change, *Journal of Biological Chemistry* (2022), doi: https://doi.org/10.1016/j.jbc.2022.102323.

manuscript_v21-BIB.docx

Dynamics of integrin α5β1, fibronectin, and their complex reveal sites of interaction and conformational change

Yang Su[1, 2, †], Roxana E. Iacob[3, †], Jing Li[1, 2], John R. Engen[3] and Timothy A. Springer[1, 2, *]

[1] Program in Cellular and Molecular Medicine, Boston Children's Hospital
[2] Departments of Biological Chemistry and Molecular Pharmacology and of Pediatrics, Harvard Medical School, Boston, MA 02115
[3] Department of Chemistry & Chemical Biology, Northeastern University, Boston, MA 02115
* Correspondence to: springer@crystal.harvard.edu
† These authors contributed equally to this work

Keywords: Integrin; fibronectin; affinity; conformational change; thermal stability; hydrogen deuterium exchange mass spectrometry; protein–protein interactions; ligand binding

Abstract

Integrin α5β1 mediates cell adhesion to the extracellular matrix (ECM) by binding fibronectin (Fn). Selectivity for Fn by α5β1 is achieved through recognition of an RGD motif in the 10th type-III Fn domain (Fn10) and the synergy site in the 9th type-III Fn domain (Fn9). However, details of the interaction dynamics are unknown. Here, we compared synergy-site and Fn-truncation mutations for their α5β1-binding affinities and stabilities. We also interrogated binding of the α5β1 ectodomain headpiece fragment to Fn using hydrogen deuterium exchange mass spectrometry (HDX MS) to probe binding sites and sites of integrin conformational change. Our results suggest the synergistic effect of Fn9 requires both specific residues and a folded domain. We found some residues considered important for synergy are required for stability. Additionally, we show decreases in fibronectin HDX are localized to a synergy peptide containing contacting residues in two β-strands, an intervening loop in Fn9, and the RGD-containing loop in Fn10, indicative of binding sites. We also identified binding sites in the α5-subunit β-propeller domain for the Fn9 synergy site and in the β1-subunit βI domain for Fn10 based on decreases in α5β1 HDX. Interestingly, the dominant effect of Fn binding was an increase in α5β1 deuterium exchange distributed over multiple sites that undergo changes in conformation or solvent accessibility and appear to be sites where energy is stored in the higher-energy, open-integrin conformation. Together, our results highlight regions important for α5β1 binding to Fn and dynamics associated with this interaction.

Introduction

Integrins are αβ-heterodimeric cell-surface receptors that sense cellular environments and mediate cell adhesion and migration. Their α and β subunits are comprised of large extracellular domains (ectodomains) that link to single-pass transmembrane domains and cytoplasmic tails. The two subunits associate noncovalently to form a ligand-binding head distal to the cell membrane (Fig. 1A). By binding glycoprotein ligands in the extracellular matrix (ECM) or on the surface of other cells and connecting to the actin cytoskeleton inside the cell, integrins transmit signals, including tensile force, between the extracellular and intracellular environments. The prototypic α5β1 integrin mediates cell adhesion to fibronectin (Fn) in the ECM; it also directs Fn fibril formation and assembly into the ECM (1,2). The interaction between α5β1 and Fn is important for vertebrate development(3) including vascular development and angiogenesis (4) and cancer progression (5).

Like most integrins, activation of α5β1 for high-affinity ligand binding is accompanied by large conformational changes in its ectodomain. α5β1 equilibrates between three overall conformations, bent-closed (BC), extended-closed (EC) and extended-open (EO) (Figure 1AB) (6-8). In the resting state on the cell surface, α5β1 is predominantly (>99%) in the BC conformation where the ectodomain bends at the knees and the lower legs and transmembrane domains in each subunit associate with one another. Extension at the knees separates the headpiece from the lower legs in each subunit (6,8-12). Headpiece opening reshapes the βI domain around the ligand-binding site, which is linked to swing-out of the β-subunit hybrid domain away from the α5-subunit thigh domain (6,12-15) (Figure 1C,D). Both BC and EC conformations are low-affinity; transition to the EO conformation increases α5β1 affinity for ligand by ~5000-fold (8). The divalent ion Mn^{2+} can activate high-affinity ligand binding *in vitro* by facilitating these conformational changes as well as increasing the intrinsic affinity of each conformation for ligand (16). In the presence of Mn^{2+}, the α5β1 headpiece was closed when unliganded and became open when an RGD peptide or Fn was bound (Fig. 1A-D) (6,12,17).

α5β1 belongs to a subfamily of integrins that recognize an Arg-Gly-Asp (RGD) sequence in their ligands. While many integrin ligands contain the RGD motif, α5β1 binding to Fn is unusual in requiring both the RGD sequence located in the 10th type-III Fn domain (Fn10) and the synergy site located in the adjacent Fn9 domain (18-22). A recent cryo-EM structure of the α5β1·Fn complex clarified this dual recognition mode by showing that the RGD-bearing loop in Fn10 is inserted in a cleft between the α5-subunit β-propeller domain and the β1-subunit βI domain while the synergy site in Fn9 contacts the α5-subunit β-propeller domain (Figure 1E), as earlier predicted (12). However, much more remains to be learned about this important interaction.

Here, we have complemented static pictures from crystal and cryo-EM structures that reveal how RGD peptides and Fn bind to integrin α5β1 with studies of how their interaction affects the backbone dynamics not only of regions that interact but also regions that undergo conformational changes. We explore the α5β1 headpiece, Fn and their interactions by using hydrogen-deuterium exchange (HDX) coupled with mass spectrometry. The integrin headpiece fragment (Fig. 1A right) contains the ligand binding site, has the same intrinsic affinity for Fn as the complete ectodomain and intact integrin on the cell surface, and undergoes the same closed to open conformational change as the complete ectodomain and intact integrin on the cell surface (8,12-14,17). HDX measures exchange of protein backbone amide hydrogens with deuterium. The exchange is sensitive to hydrogen bonding, solvent accessibility, and backbone movement, and thus reports local backbone conformation and dynamics (23). HDX measurements provide

unique insight into the dynamics of proteins and protein–protein interactions and are complementary to structural methods such as crystallography and EM that provide snapshots of low energy positions of proteins within their energy landscapes. To understand how motions in fibronectin integrin-binding fragments (ligand) and fibronectin-binding integrin headpiece fragments (receptor) change upon complex formation, we have studied here HDX in the ligand, the receptor, and their complex. To complement this work, we have also studied how ligand-binding affinities vary in mutants and Fn domain truncations.

Results

Dynamics, stability, and affinity for α5β1 of Fn fragments and mutants

We describe, in turn, deuterium uptake dynamics in fibronectin fragments, then in the integrin α5β1 headpiece fragment, and then in integrin α5β1 headpiece complexes with fibronectin fragments and RGD peptide (Supplementary Table S1). We first measured HDX for Fn9–10 (30 peptides constituting 97.3% sequence coverage) and Fn7–10 (32 peptides constituting 69.8% sequence coverage) in the absence of α5β1 integrin. The individual Fn domains showed distinct deuterium uptake profiles (Figure 2A-D, Supplementary Figure S1). Fn7 and Fn10 incorporated the highest amount of deuterium; in most regions more than 50–60% of available amide hydrogen atoms were exchanged with deuterium after 4 hr. Importantly, the integrin-binding RGD loop in Fn10 had high exchange (Figure 2E), showing that it is highly dynamic in agreement with NMR studies on Fn10 and Fn9–10 fragments (24,25). Fn9 incorporated less deuterium compared to Fn10 in the Fn9–10 fragment, even though as isolated domains Fn9 was less stable than Fn10 by differential scanning calorimetry and chemical denaturation studies (26,27). Most Fn9 peptides showed less than 50% exchange after 4 hr. The synergy site in Fn9 was notably one of the least exchanging regions and exchanged only ~35% after 4 hr (Figure 2A-D and F).

The Fn9 domain was more dynamic in Fn9–10 than in Fn7–10. In particular, the Fn9 B-C loop, which contacts the Fn8 domain, incorporated more deuterium in Fn9–10 than in Fn7–10, particularly at early time points (Figure 2G). Correlating with this difference in HDX, Fn8 stabilized Fn9 and Fn10 in thermal unfolding experiments measured by intrinsic tryptophan fluorescence (Figure 3A).

The Fn7, Fn8, Fn9, and Fn10 domains each contain a single Trp residue that is buried in the hydrophobic core. In general, tryptophan fluorescent emission shifts from ~330 nm to ~350 nm as a result of increased solvent exposure during unfolding. Instead of stepwise transitions for each individual Fn domain, a single transition was observed for Fn9–10, Fn8–10 and Fn7–10 that suggested cooperative thermal unfolding for the less stable Fn8 and Fn9 domains (26,27). The T_m's of Fn8–10 and Fn7–10 (Figure 3A) were comparable and were 8 °C higher than that of Fn9–10, showing that Fn9 and Fn10 are stabilized by Fn8, and that Fn7 did not provide further stabilization. In agreement with previous reports on isolated Fn domains, the T_m of Fn10 was high (26,27); however, its "folded" and "unfolded" states showed substantially higher F350/F330 fluorescence ratios than the corresponding states of the tandem domains in Fn9–10, Fn8–10 and Fn7–10 (Figure 3B). These differences suggest that the folded and unfolded states of Fn10 may each be more disordered than those in the fragments with tandem domains.

We next compared the importance of Fn domains 8, 9, and 10 and the synergy site for binding in Ca^{2+}/Mg^{2+} to a WT and mutant α5β1 integrin. The mutation is in a residue that interacts with the synergy site, α5 D154A ($\alpha5^{D154A}\beta1$) (Figure 1E). Affinity of the α5β1 ectodomain for Fn was measured by competition with a fluorescently labeled fibronectin-mimetic RGD peptide cyclized with a disulfide bond, ACRGDGWCG (cRGD) (28,29), in

fluorescence anisotropy. The affinities of WT α5β1 for Fn9–10 and Fn8–10 were within experimental error of one another; however, affinities of both Fn9–10 and Fn8–10 were substantially higher, by 20–30-fold, than that of Fn10 (Figure 3CD and Supplementary Fig.2), consistent with the synergy site in Fn9 augmenting binding affinity for α5β1 (18-22). Thus, the addition of Fn9 to Fn10 raised affinity for α5β1 by ~25-fold over Fn10 alone, placing a quantitative value on the affinity enhancement by Fn9 and its synergy site. Furthermore, HDX showed that Fn9 was more stable in Fn7–10 than in Fn9–10 and T_m values showed that Fn7–10 and Fn8–10 were comparably stable and that Fn9–10 was less stable. However, because Fn8–10 and Fn9–10 have similar binding affinities for α5β1, these results suggest that the stability of Fn9–10 is sufficient for maximal binding affinity for α5β1.

To better understand the role of the synergy site, a single-residue mutation of Arg-1379 to Ala (Fn^R) and a triple mutation of residues Arg-1374, Pro-1376 and Arg-1379 to Ala (Fn^{RPR}) were created in Fn8-10 and Fn9-10. Previously, structures of Fn7–10 and the α5β1 headpiece bound to an RGD peptide, together with docking and mutation of acidic residues in the α5 β-propeller domain and Arg-1379 in the Fn9 domain, suggested that Asp-154 in the α5 β-propeller domain bound to Arg-1379 in the Fn9 domain (13) as later confirmed by cryo-EM (12) (Figure 1E). We found similar 3-fold decreases in affinity of WT α5β1 for Fn^R9–10 and Fn^R8–10 and of WT Fn9–10 and Fn8–10 for $\alpha5^{D154A}\beta1$ (Figure 3D and Supplementary Figure S2). Furthermore, there was little or no further decrease in affinity of $\alpha5^{D154A}\beta1$ for the Fn^R mutants of Fn9–10 and Fn8–10, supporting the interaction of α5 Asp-154 with Fn Arg-1379. The more drastic Fn^{RPR} triple mutant lowered affinity by 15 to 17-fold of Fn9–10 and Fn8–10 for WT α5β1. The decrease in affinity of the Fn8-10^{RPR} and Fn9-10^{RPR} mutants was similar for α5β1 and $\alpha5^{D154A}\beta1$, as expected from the interaction of α5 Asp-154 with Fn Arg-1379 (13). However, the similarity in affinity of α5β1 for Fn^{RPR}Fn9–10, Fn^{RPR}8–10, and Fn10 (Figure 3D) was unexpected. The α5β1 / Fn9-10 complex structure shows that Arg-1374 has no interaction with α5β1 and that Pro-1376 lacks a van der Waals interaction with α5β1 and buries only slightly less solvent accessible surface area (15 $Å^2$) than the Ala-1376 mutant (assuming the mutation does not perturb backbone conformation) (12). Furthermore, interactions between Fn and α5β1 extend beyond the synergy site to include, for example, a salt bridge between α5 Lys-125 and Fn Asp-1373 (Fig. 1E). These results suggest that the Fn^{RPR} mutation may alter the structure of Fn9 and largely disable its interaction with α5β1.

Did the Fn^{RPR} or Fn^R mutations in Fn9 directly alter interactions with α5β1, or cause unfolding or a change in structure of Fn9 so it no longer interacted? To examine unfolding, we measured the stabilities of the Fn^{RPR} and Fn^R mutants in thermal and urea denaturation (Figure 3A,B). The T_m's of Fn9–10 and Fn^R9–10 were similar, while the T_m of Fn^{RPR}9–10 was 4 °C lower. Unfolding in urea showed that the folding free energy of Fn^R9–10 was increased by 0.4 kcal/mol; thus, while removal of the sidechain of Arg-1379 decreases interaction with α5β1, removal stabilizes Fn9-10 folding. In contrast, the folding free energy of of Fn^{RPR}9–10 was decreased by 0.5 kcal/mol relative to WT and by 0.9 kcal per mole relative to Fn^R9–10. These differences are consistent with a change in structure of Fn9 in the Fn^{RPR} mutation.

In HDX experiments on Fn complexes with α5β1, it is important to know the populations of the conformational states of bound and unbound α5β1 headpiece and to calculate the percent of the α5β1 headpiece bound to Fn. We used the α5β1 headpiece to simplify peptide analysis in HDX; HDX was performed initially with the ectodomain but there were difficulties in reduction and digestion of the disulfide-rich lower leg of β1. The headpiece contains the ligand binding domains and lacks the lower legs of the ectodomain (Figure 1A). In Mg^{2+}/Ca^{2+}, the α5β1

headpiece is 99.97% in the closed conformation and 0.03% in the open conformation based on previous accurate measurements of its conformational equilibria (8). To maximize integrin binding to fibronectin, all HDX measurements on α5β1 bound to fibronectin and cRGD were done in the presence of Mn^{2+} instead of Mg^{2+}/Ca^{2+}, which increases intrinsic affinity for ligand ~30-fold and also increases population of the high-affinity, open conformation (16). To determine the completeness of binding in Mn^{2+}, we measured the affinities of cRGD and Fn7–10 and Fn9–10 for the α5β1 headpiece in Mn^{2+}. The results with Fn7–10 and Fn9–10 were similar, and showed affinities in Mn^{2+} of ~0.5 nM for the basal ensemble and ~30 nM for the closed state (Supplementary Fig. S3). cRGD binds to the basal ensemble of the α5β1 headpiece in Mn^{2+} with an affinity of 3.2±0.3 nM. In Mn^{2+}, the intrinsic affinities of cRGD for the closed states of the α5β1 headpiece of 44±3 nM and the ectodomain of 46±5 nM are similar (16), in agreement with the previously established concept that integrin affinities are intrinsic to conformational states and independent of whether the integrin is on the cell surface or a particular fragment (8,30). Using this concept, data from Supplementary Fig. S3, other measurements (16), and the equations described in Methods, we calculated the extent of binding and the conformational composition of each of the HDX samples described below (Tables S2 and S3). The results showed that the ligand binding site on α5β1 was more than 99.66% occupied with all three ligands and that α5β1 was 93% open and 7% closed when bound to cRGD and 97–98% open and 1–2% closed when bound to Fn9–10 and Fn7–10.

To map the effects on Fn of binding to α5β1, we measured deuterium incorporation for Fn9–10 and Fn7–10 fragments in complex with α5β1 and compared those values to deuterium incorporation of Fn9–10 and Fn7–10 alone, under identical HDX MS conditions. Most Fn peptides did not show a meaningful difference in deuterium uptake ($|\Delta D| > 0.7$ Da) between α5β1-bound Fn and free Fn (Figure 4 and Supplementary Figure S4). However, α5β1 protected RGD loop and synergy site peptides. The RGD-bearing loop (residues 1488–1509) in Fn9–10 and Fn7–10 incorporated less deuterium across all time points when bound to α5β1 (Figure 4C). The synergy site peptide, which was covered in Fn9–10 but not in sparsely covered Fn7–10 (Figure 4A), also incorporated less deuterium at all time points in presence of α5β1 (Figure 4D).

Dynamics of unliganded and liganded α5β1 integrin.

HDX MS was performed on the unliganded α5β1headpiece, and the headpiece in complex with cRGD peptide, Fn9-10 , or Fn7-10 (Supplementary Figure S5-8). For the unliganded α5β1headpiece, deuterium uptake was below 50% after 4 hr in most regions (Figures 5A and 6). In particular, the core of the β-propeller domain showed <30% exchange even after 4 h, consistent with the fact that the β-strands that form the propeller blades are extensively hydrogen-bonded. Among the four large domains in the headpiece, the thigh domain showed more exchange overall than the other three domains (Figure 5). Within the domains, a few isolated regions showed more extensive exchange (>50% at 4 h). The W-A loop in the hybrid domain exchanged the most (>80% at 4 h) (Figures 5 & 6H), consistent with the disordered loop observed in some crystal structures (14). In the βI domain, the ligand-proximal α1-helix, the α1′ helix, and the specificity-determining loop 2 (SDL2) exchanged extensively (>50% at 4 h) (Figures 5 & 6I-K).

To map the effects of ligand binding on α5β1, we measured α5β1 deuterium uptake in the same Fn9–10 and Fn7–10 complexes with α5β1 that were described in the previous section. Additionally, the α5β1 headpiece was complexed with cRGD. Comparing HDX of α5β1 in the ligand-bound form to the unbound form revealed deuterium uptake differences ($\Delta D = D_{\text{bound } \alpha5\beta1} - D_{\text{free } \alpha5\beta1}$) both at and distal to the ligand-binding site. Changes in deuteration greater than 0.7

Da (increases, pink-dark red) or less than 0.7 Da (decreases, cyan-blue) in peptides are shown on the structures in Figure 7. Altered HDX reflects both the effects on specific regions of α5β1 that bind to ligand and the effects of conformational change from the closed to the open conformation. Under the conditions of our HDX experiments in the presence of Mn^{2+}, the α5β1 headpiece changed from 0.4±0.2% open in the absence of ligand to 93–98% open in the presence of the three ligands (Supplementary Table S3). All HDX mass spectra displayed a single binomial isotope distribution, indicative of a single population of molecules in solution, that increases in mass with longer deuteration time (EX2 kinetics (31)). No peptides showed a bimodal distribution where the lower mass distribution reflects a more protected less deuterated species and the higher mass distribution a less protected more deuterated species, a hallmark of simultaneously existing populations in distinct conformational states (EX1 kinetics (31)). These findings would be consistent with both the calculated predominance of the open integrin state in presence of ligand and the closed state in absence of ligand, as well as interconversion between closed and open states on a timescale more rapid than our HDX experiments.

Interconversion between the open and closed conformations of integrin α5β1 is regulated by alterations in the βI domain and its interface with the hybrid domain. The three regions of the integrin βI domain that move the most in allostery are the α1-α1′, α2, and α7 helices (32) (Figures 6I-K,M,P and 7A,B,D). All three ligands uniformly increased HDX of the α2 and α7 helices. In contrast, effects of the ligands differed on the α1-α1′ helix. A large number of peptides covered the combined α1-α1′ helix, including 131–160, which showed an increase in HDX by cRGD and not Fn9–10 or Fn7–10 (Figure 6I and Supplementary Figure S9). Greater insight was provided by peptides 134–149 (α1-helix) and 150–160 (α1′ helix) (Figures 6J and 6K, respectively). cRGD enhanced exchange in α1, while Fn9–10 and Fn7–10 only slightly increased α1 exchange. In contrast, all three ligands similarly and slightly decreased exchange in α1′. In the open conformation of the βI domain, the β-MIDAS motif that coordinates the MIDAS and ADMIDAS metal ions, which largely is within the α1-helix, moves and forms enhanced interactions with the MIDAS Mg^{2+} ion, the ADMIDAS Ca^{2+} ion, and the Asp of the RGD motif present in all three ligands (15,32).

The increase in HDX of the α1-helix is the opposite of that expected from stabilization and burial by ligand binding. Instead, the increase in exchange in the α1, α2, and α7 helices correlates with the lower stability of the α5β1 headpiece in the open conformation—by 4.7 kcal/mol compared to the closed conformation (8). The lesser increase in exchange of the α1-helix by the two Fn fragments than cRGD may be accounted by their larger burial of the α1-helix; for example, Tyr-1446 of the Fn10 domain hydrogen bonds to βI residue Asp-137, which is part of the α1-helix and coordinates the ADMIDAS Ca^{2+} ion (Figure 1E).

Other regions of altered HDX in the β1 subunit were in βI and hybrid domain interfaces. The α3-β4 and α5-β5 loops in the βI domain and F-G loop in the hybrid domain in the βI-hybrid domain interface all showed increased HDX in the presence of ligand (Figures 6N,O,R & 7A,B,D). The C-D loop in the hybrid domain is in a contact with a long β-ribbon in the β-propeller domain in the closed conformation that is broken in the open conformation, correlating with increased HDX in presence of the three ligands (Figure 1C,D, 6Q, and 7A,B,D). SDL2 shows an increase in HDX at early time points in liganded α5β1 (Fig. 6L), correlating with its movement together with the contacting Tyr-133 sidechain in the α1-helix, which contacts Pro-1497 in the Fn10 RGD loop.

Ligand binding-dependent HDX signatures were fewer in α5 than in the β1-subunit but provided important insights. The W2β4-W3β1 loop (peptide 148–168) in α5, which contains

Asp-154 that binds to Fn9 synergy site residue Arg-1379, showed decreased HDX with both Fn9–10 and Fn7–10 at later time points, confirming the importance of the synergy site (Figure 6A and 7A-C). Interestingly, cRGD decreased exchange somewhat more in the same peptide. cRGD gains high affinity for α5β1 from the Trp residue in position 7 of its sequence, ACRGDGWCG, which was predicted to interact with α5 Trp-157 by mutagenesis (28,29). Indeed, a crystal structure shows a T-shaped interaction between Trp-7 of cRGD and α5 Trp-157 with formation of two π–π bonds (14), explaining the decrease in deuteration upon cRGD binding. In contrast, peptides containing Asp-227 in the α5 β-propeller W3β4-W4β1 loop, which forms bidentate hydrogen bonds to the Arg sidechain of the RGD moiety of the three ligands, did not show changes in HDX (Figure 6C). This may be because Asp-227 lies in a cleft (Figure 1E) and was already quite stable owing to a pre-existing hydrogen bond network that includes its sidechain and the presence of at least one mainchain-mainchain hydrogen bond in Asp-227 and its flanking residues from positions 223 to 231.

Two other regions of the α5 β-propeller showed lower exchange upon ligand binding. The β-ribbon in the β-propeller domain, which contacts the C-D loop in the hybrid domain in the closed but not open conformation, as already discussed above, showed increased deuterium uptake upon ligand-binding at early time points (10 s and 1 m) (Figures 6D & 7ABC). Interestingly, increased exchange at the 10 s and 1 m and not later time points was seen for both the β-ribbon and C-D loop (Figure 6D,Q), suggesting that whereas ligand-binding resulted in headpiece opening and broke cognate interactions between these regions at early timepoints, their interface was also susceptible to breathing motions in the closed conformation that resulted in exchange at later timepoints. A long peptide in the thigh domain (549–585) showed HDX that was increased by ligand binding by ~2–3 Da at all time points (Figures 6F & 7ABC). Lack of differences in overlapping peptides 546–555 and 556–569 (Figure 6E&G & Supplementary Figure S9B) suggested that the increase in deuteration occurred in residues 570–585 in the thigh domain F-G loop. The F-G loop has an extensive interface with the β-propeller domain (Figure 7AB). Studies of integrin ectodomains with multiple examples in crystal lattices have shown differences of up to 20° in thigh/β-propeller domain orientation (33). The thigh domain is close to the PSI domain in the closed conformation; loss of contact with PSI in the open conformation may alter thigh/β-propeller domain orientation and is one possible explanation for increased exchange of the thigh F-G loop in the open conformation. Another possibility is transmission of energy from the ligand binding-interface through the relatively rigid β-propeller domain to its interface with the thigh domain.

Discussion

The seminal observation by Ruoslahti and colleagues that the RGD motif in fibronectin was sufficient to bind integrin α5β1, and was also recognized by other integrins in other extracellular ligands, raised the question of how specificity was obtained (34). Yamada and colleagues answered this question for α5β1 by demonstrating recognition of a distinct, synergistic site in Fn9 that neighbored the Fn10 domain bearing RGD (18,19). Structures of α5β1 complexes by the groups of Takagi and Mizuno (12,13) have clearly shown how the Fn9 domain is bound, but questions remain. For example, it has been suggested that synergy site mutations act indirectly by decreasing Fn9 stability, and a stabilizing L1408P mutation on the non-bound face of Fn9 was shown to increase α5β1 affinity for Fn9–10 (22).

We have determined equilibrium binding affinities for synergy site mutations and Fn fragments of different lengths and their stabilities using thermal and urea denaturation. Although our results on the Fn9 Arg-1379 interaction with α5 Asp-154 are confirmatory, we believe that

they are the first true affinity measurements. We find only a ~3-fold reduction in affinity with the Fn9 R1379A and α5 D154A mutations alone or their combination. In contrast, competition of cell adhesion by R1379A Fn9–10 fragments showed a 70–100-fold reduction in potency (19,21). Previous measurements by ELISA used washing and were thus inherently not in equilibrium; previous SPR measurements were not fit globally to demonstrate 1:1 Langmuir binding; furthermore, both methods use solid phases which introduce biases not found in solution binding assays. One study reported apparent affinities (EC_{50} values) in ELISA and SPR that differed internally from one another by 10-fold for some mutants and 5-fold for another, nonetheless, the relative differences between WT and R1379A Fn9–10 were close to the three-fold difference found here (22). The three residues in Fn found most important for synergy were combined here in the triple mutant R1374A/P1376A/R1379A (Fn^{RPR}) (19,21). The Fn^{RPR} mutant lowered affinity by 15–17 fold, almost as much as seen with the 20–30-fold decrease in affinity with omission of the Fn9 domain. The same Fn^{RPR} mutant studied by the Takagi group was found to decrease EC_{50} by ~30-fold, in good agreement with our results (13).

Subsequent structure determination showed that Arg-1374 points away from α5 and that Pro-1376 is on the periphery of the contact and buries only a small amount of solvent-accessible surface area (12), supporting the idea that the R1374A and P1376A mutations might lower Fn9 stability or alter its structure and thus indirectly affect affinity. Our stability measurements and the similar affinities for α5β1 of Fn^{RPR}9–10 and Fn10 support this idea. We found single thermal and urea denaturation transitions for Fn7–10, Fn8–10, Fn9–10, and Fn10 fragments. Fn7 and Fn10 are very stable and the single transitions in other fragments likely reflect unfolding of the less stable Fn8 and Fn9 domains (22,26). The Fn^{R} 9–10 mutant was more stable than WT in urea, as also found for Fn^{R}9–10 in guanidine (22). In contrast, the Fn^{RPR} mutant was substantially less stable than WT, showing that only the R1374A and/or P1376A mutations are detrimental to stability. These results suggest that the predominant effect of the R1374A and P1376A mutations is to disrupt the structure of Fn9 so that it binds α5β1 less well.

In conclusion, it appears that previous attempts to define a synergy site within Fn9 identified both a specific contact of Fn9 Arg-1379 with α5 Asp-154 that decreased affinity by 3-fold, and other residues that decreased affinity substantially more by altering the folding or structure of Fn9. Although one group suggested that synergistic activity depended on structural stability, it is interesting that they found one exception to this trend: R1379A (Figure 5 in (22)). It was noble to attempt to identify a synergy site motif in Fn9 that could be distilled down to a short amino acid sequence like RGD in Fn10 (18,19,21); however, our data and recent structures (12,13) suggest that the folded structure of Fn9 and residues that are distant in sequence but close in structure are required for proper recognition by α5β1. Thus, it appears more correct to think of Fn9 as being a synergistic domain rather than to think of Fn9 as containing a synergistic site that can be reduced to a sequence motif analogous to RGD.

Our HDX experiments showed integrin α5β1-binding signatures in Fn7–10 and Fn9–10 only of peptides 1373–1384 in Fn9 and 1488–1509 in Fn10. It is important to point out that peptide 1373–1384 contains multiple residues within van der Waals distance of α5β1 including the sidechains Asp-1373, Arg-1379, Ser-1381, and the backbone of Ile-1382, and that these residues are in two β-strands and the loop between them and thus require an intact Fn9 domain for their proper 3-dimensional organization into a binding surface (12). Peptide 1488–1509 contains only three residues in van der Waals contact with α5β1, Arg-1493, Asp-1495, and Pro-1497; these residues are at the tip of the long RGD loop and therefore have little dependence on the remainder of the Fn10 domain for their 3-dimensional organization. These differences

correlate with the domain-like and sequence motif-like characters of α5β1 binding by Fn domains 9 and 10, respectively.

In α5β1, we saw an HDX signature for binding of Asp-154 to Arg-1379 in Fn9 in the decreased exchange of α5 peptide 148–168 (W2β4-W3β1 loop). We did not see a signature for binding of Arg-1493 in the RGD motif of Fn10 to Asp-227 in the α5 β-propeller domain. As discussed in Results, the lack of decreased HDX may be because the Asp-227 sidechain and the mainchain of residues 223 to 231 in the polypeptide chain are secured by hydrogen bonds, and thus mainchain exchange may already be low prior to Fn binding.

An unexpected increase of large magnitude in HDX was seen in the thigh domain F-G loop, which is in intimate contact with the α5 β-propeller domain. The thigh domain may act as a chaperone for folding of integrin β-propellers, because no integrin has ever been successfully biosynthesized and expressed as a recombinant αβ heterodimer containing only the β-propeller domain in the α-subunit, despite the ability to proteolytically remove the thigh domain after biosynthesis with full retention of ligand-binding activity (32). The α5 β-propeller domain is knitted together by association of residues 1–12 containing β-propeller β-strand 4 with β-strands 1–3 formed by residues 410–452 into β-sheet (blade) 7 of the 7-bladed β-propeller domain (35). The thigh F-G loop lines the interface with β-sheet 7 of the β-propeller domain, contacts both the N-terminal segment prior to β-strand 1, the connection to the thigh domain through the segment after β-strand 4, and the loop between β-strands 2 and 3. Thus the thigh F-G loop may chaperone the β-propeller by helping to splice together its N and C-terminal portions. Movement of the PSI domain in the upper β-leg away from close proximity to the thigh domain and its impact on motions at the thigh–β-propeller interface at the F-G loop is one possible explanation for its increased HDX as mentioned in the Results section. Another possible explanation would be transmission of motion through the β-propeller domain from its ligand binding interface with the βI domain to the thigh F-G loop; specific pathways for transmission of allostery and motion through domains have been observed in model systems (36).

Binding of Fn7–10, Fn9–10, and cRGD peptide to α5β1 strikingly altered HDX in all β1 subunit regions with conformational change upon opening (12,15,32), including the βI domain α1 and α1′ helices. In opening, these helices move toward the ligand binding site and the α1 helix contacts ligand, including forming mainchain hydrogen bonds to the sidechain of the Asp of RGD. Upon opening, the α1 and α1′ helices, which are separated by a bend in the closed conformation, fuse to form a single straight helix. Binding of cRGD increased exchange in the α5β1 βI domain α1 helix substantially more than Fn7–10 and Fn9–10, consistent with burial of α1 helix residues D137–E140 by non-RGD portions of Fn including formation of a hydrogen bond from Fn Tyr-1446 to the Asp-137 sidechain; the other carboxyl oxygen of the Asp-137 sidechain coordinates the ADMIDAS Ca^{2+} ion. It appeared that conformational change upon binding to RGD in all ligands substantially increased exchange in the α1-helix and that this was partially offset by stabilizing interactions formed by non-RGD portions of the Fn10 domain in Fn7–10 and Fn9–10 that lowered exchange. On the other hand, exchange in the α1′ portion of the merged α1/α1′-helix in the βI domain was decreased by binding of all ligands, perhaps by helix merger.

All other regions of the α5β1 headpiece that alter conformation upon headpiece opening showed ligand-binding induced increases in HDX. The α2 and α7-helices in the βI domain lie on opposite sides of the α1-helix and show piston-like movements in allostery. Each showed dramatic increases in deuteration after ligand binding, which stabilized almost complete conversion of ligand-bound α5β1 to the open conformation as shown by energy landscape

measurements and calculations. Two loops each in the βI domain and in the hybrid domain showed more deuteration after ligand binding. Three of these loops were at the interface between the βI and hybrid domains, which undergoes a large change in inter-domain orientation upon opening. Regions of the β-propeller and hybrid domains that touch in the closed but not open conformations also showed increased HDX. The HDX results thus define many regions that are less stable in the open than the closed conformations. Measurements of the free energy on the closed and open states of the α5β1 headpiece fragment show an increase of 4.7 kcal/mol in the open state (8). Our findings thus highlight critical regions in the α5β1 headpiece where this increase in energy in the open conformation is likely to be stored.

In conclusion, our results add much to our understanding of how integrin α5β1 binds fibronectin and how stabilization of the open conformation by ligand binding alters integrin dynamics. Affinity measurements and stability measurements on WT and mutant fibronectin fragments show that both the Fn9 and Fn10 domains make important contributions to affinity for α5β1. A well-folded Fn9 domain and its Arg-1379 sidechain are required for full affinity; however, other residues that were thought to be part of a synergy site appear to stabilize folding of Fn9 rather than to contribute specific contacts as previously suggested. Owing to the prescient modeling of Fn-α5β1 interaction based on an α5β1 RGD peptide crystal structure (13) and a cryoEM structure of a fibronectin fragment bound to α5β1 (12), our work added little information on where fibronectin and α5β1 bind to one another.

Comparison of the α5β1 headpiece alone, which was almost completely in the closed conformation, to the fibronectin-bound α5β1 headpiece, which was almost completely in the open conformation, revealed interesting information on changes in integrin dynamics upon conformational change. Binding of the Fn10 domain to the βI domain α1-helix backbone and sidechain was accompanied by an increase in α1-helix dynamics. Normally, HDX decreases in binding sites; therefore, the increase in HDX was attributed to the known conformational change in the α1-helix between the closed and open states in α5β1. This was supported by the greater increase in HDX in α5β1 when bound to a cyclic RGD peptide, which induces the same open state of α5β1 (8) yet buries less of the α1-helix in its complex. Merger of the α1-helix with the α1'-helix in the open conformation was accompanied by a decrease in HDX. All other regions involved in conformational change showed increased HDX, including α-helices that undergo connecting rod-like movements in the βI domain, loops in the βI domain and the hybrid domain at their shape-shifting interface, and contacts between the α and β-subunits. The increase in HDX showed that these regions were more dynamic, i.e. had higher energy, in the open than the closed conformation. In agreement, measurements of the free energy of the closed and open states of the same α5β1 headpiece fragment show an increase of 4.7 kcal/mol in the open state (8). Thus, our HDX measurements highlight, at least in part, regions in the α5β1 headpiece where this increase in energy in the open conformation is stored. We believe it is interesting that this energy is distributed in multiple regions throughout the βI and hybrid domains rather than concentrated. This distribution might serve to lower the energy of the transition state between the two states, thus increasing the likelihood of the transition and the kinetics of conformational change. Distribution might also serve to decrease the likelihood of denaturation of a specific portion or the entirety of a domain. These results thus provide important insights into integrin conformational change that are orthogonal and complementary to insights from previous structural and thermodynamic studies.

Experimental Procedures

Proteins and cRGD peptide. α5β1 headpiece and ectodomain (mature residues α5 F1–L609/β1 Q1–E481, and α5 F1–Y954/β1 Q1–D708, respectively) were expressed in HEK 293S GnTI$^{-/-}$ cells and purified as described (14). The α5 D154A mutant of α5β1 ectodomain ($\alpha5^{D154A}\beta1$) was expressed in Expi293F GnTI$^{-/-}$ cells and purified in the same way. Fibronectin fragments Fn10, Fn9–10, Fn8–10, and Fn7–10 (mature residues V1416–T1509, G1326–T1509, T1265–T1509, and P1142–T1509, respectively) and their associated synergy site mutants R1379A (Fn^{R}) and R1374A/P1376A/R1379A (Fn^{RPR}) were expressed in *E. coli* BL21(DE3) cells and purified as described (37). The cyclic peptide ACRGDGWCG (> 95% pure) was synthesized by GenScript. To form α5β1·Fn9–10 and α5β1·Fn7–10 complexes, α5β1 headpiece was incubated with 2-fold molar excess of Fn9–10 or Fn7–10 for at least 20 min at 23°C in 20 mM Tris buffer pH 7.4, 150 mM NaCl, 2 mM $MnCl_2$ and 0.2 mM $CaCl_2$. The complexes were then isolated by size-exclusion chromatography.

Fluorescence polarization (FP). Saturation binding was performed with 10 nM FITC-cRGD probe and varying concentrations of α5β1 headpiece or ectodomain. Competitive binding was performed with 100 nM α5β1 headpiece or α5β1 ectodomain, 10 nM FITC-cRGD probe and varying concentrations of Fn9–10 or Fn7–10. Binding was in 20 mM Tris buffer pH 7.4, 150 mM NaCl, supplemented either with 1 mM $MgCl_2$ and 1 mM $CaCl_2$, or with 2 mM $MnCl_2$ and 0.2 mM $CaCl_2$, as indicated. The mixture was allowed to equilibrate at 22°C for 2 h before recording FP on a Synergy NEO HTS multi-mode microplate reader (Biotek). Experiments were performed in triplicate unless otherwise indicated.

Thermal stability. Thermal denaturation was measured with a Prometheus NT.Plex (NanoTemper Technologies). Fn7–10, Fn8–10 and Fn9–10 (1 mg/mL) in 20 mM Tris buffer pH7.4, 150mM NaCl were heated from 20 °C to 95 °C at a rate of 1 °C/min. Intrinsic tryptophan fluorescence was excited at 275 nm and emission was monitored at 350 nm and 330 nm. The ratio of fluorescence intensities (F350/F330) is plotted as a function of temperature. T_m is defined as the temperature at the inflection point of the curve.

Chemical denaturation. Fn10, Fn9–10, Fn^{R}9–10 and Fn^{RPR}9–10 (0.2 mg/mL) were equilibrated in 20 mM Tris pH 7.4, 150 mM NaCl and indicated urea concentrations for 48 hours at 20°C. Intrinsic tryptophan fluorescence were measured at 330 nm and 350 nm upon excitation at 275 nm on a Prometheus NT.Plex (NanoTemper Technologies). The ratio of fluorescence intensities (F350/F330) was fit as a function of urea concentration to a 2-state transition model using the Linear Extrapolation Method (38):

$$F350/F330 = \frac{\alpha_N + \beta_N c + (\alpha_D + \beta_D c)\exp\left(-\frac{\Delta G - mc}{RT}\right)}{1 + \exp\left(-\frac{\Delta G - mc}{RT}\right)}$$

where Δ*G* is the unfolding free energy in the absence of urea; *c* is the concentration of urea; *m* is the cooperativity of transition from the native state (N) to the denatured state (D); *R* is the gas constant; *T* is absolute temperature; α_N, β_N, α_D and β_D are the *y*-intercept (α) and slope (β) of the baseline of the native (N) and denatured states (D), respectively. Data for Fn9–10, Fn^{R}9–10 and Fn^{RPR}9–10 were fit with shared *m* because their increase in solvent-exposed surface upon unfolding is similar (39).

Hydrogen deuterium exchange mass spectrometry. HDX MS studies were performed using methods modified from those reported previously (40). In addition to the descriptions below, comprehensive experimental details and parameters are provided in Table S1 and the Supplemental Datafile, in the recommended (41) tabular format. Relative deuterium levels and

percent deuteration values for all peptides described in both figures and text are provided in the Supplemental Datafile. The HDX MS data have been deposited to the ProteomeXchange Consortium via the PRIDE partner repository (42) with the dataset identifier PXD031508.

Deuterium exchange was measured for the following samples: α5β1 headpiece (74.5 μM), Fn9–10 (68.6 μM), Fn7–10 (65.2 μM), α5β1 (59.6 μM) + cRGD (119.2 μM) mixture, α5β1·Fn9–10 complex (47.3 μM), and α5β1·Fn7–10 complex (54.4 μM). Samples (2 μL) were diluted 15-fold into 20 mM Tris, 150 mM NaCl, 2 mM $MnCl_2$ and 0.2 mM $CaCl_2$, 99% D_2O (pD 7.4) at 21 °C. At deuterium exchange time points from 10 s to 4 h, an aliquot was quenched by adjusting the pH to 2.5 with an equal volume of 4 M GnHCl, 200 mM sodium phosphate, 0.5 M tris(2-carboxyethyl)phosphine hydrochloride (TCEP-HCl), H_2O and digested offline with pepsin for 5 min on ice prior to UPLC separation.

Mass spectrometry (MS) analyses were performed with a Synapt-G2-S*i* coupled to a nanoAcquity HDX Manager (Waters) (43). PLGS 3.0 and DynamX 3.0 were used to identify the peptides and to measure deuterium incorporation. All comparison experiments were done under identical experimental conditions such that deuterium levels were not corrected for back-exchange and are therefore reported as relative (23). The error of measuring the mass of each peptide was ± 0.15 Da or less in this instrumental setup. Each experiment was performed in at least duplicate (see Table S1). All replicates of a given dataset were merged to a single DynamX file and the error bars in uptake graphs indicate the spread of the data as provided by the DynamX software, which in most cases also includes measurements from more than one charge state of any given peptide in any given replicate.

Equilibrium populations of α5β1 headpiece. The percentage of α5β1 headpiece bound to ligand and the percentages of α5β1 in the closed or open conformations in the HDX samples were calculated according to the following equations.

(Eq. 1) $$C \rightleftharpoons O \qquad K_{conf}^{C \rightleftharpoons O} = \frac{[O]}{[C]}$$

(Eq. 2) $$C{\cdot}L \rightleftharpoons C + L \qquad K_d^C = \frac{[C][L]}{[C{\cdot}L]}$$

(Eq. 3) $$O{\cdot}L \rightleftharpoons O + L \qquad K_d^O = \frac{[O][L]}{[O{\cdot}L]}$$

(Eq. 4) $$C{\cdot}L + O{\cdot}L \rightleftharpoons C + O + L \qquad \frac{1}{K_d^{ens}} = \frac{[C{\cdot}L] + [O{\cdot}L]}{([C] + [O])[L]} = \frac{1}{K_d^C}\left(\frac{1}{1 + K_{conf}^{C \rightleftharpoons O}}\right) + \frac{1}{K_d^O}\left(\frac{K_{conf}^{C \rightleftharpoons O}}{1 + K_{conf}^{C \rightleftharpoons O}}\right)$$

(Eq. 5) $$[C] + [C{\cdot}L] + [O] + [O{\cdot}L] = [\alpha5\beta1]_{total}$$

(Eq. 6) $$[L] + [C{\cdot}L] + [O{\cdot}L] = [L]_{total}$$

(Eq. 7) $$\%\ \text{bound}\ \alpha5\beta1 = \frac{[C{\cdot}L] + [O{\cdot}L]}{[\alpha5\beta1]_{total}}$$

(Eq. 8) $$\%\ \text{closed complex} = \frac{[C{\cdot}L]}{[\alpha5\beta1]_{total}}$$

(Eq. 9) $$\%\ \text{open complex} = \frac{[O{\cdot}L]}{[\alpha5\beta1]_{total}}$$

Eq.1 describes the conformational equilibrium between the closed (C) and open (O) conformations of α5β1 headpiece in the basal conformational ensemble. A ligand (L) can bind each conformation in the ensemble to form the closed complex (C·L) and the open complex (O·L) with intrinsic affinities K_d^C and K_d^O, respectively (Eqs.2–3). Eq.4 relates the affinity of the basal ensemble (K_d^{ens}) to the intrinsic affinities (K_d^C and K_d^O) and the conformational equilibrium ($K_{conf}^{C \rightleftharpoons O}$), which provides a way to determine $K_{conf}^{C \rightleftharpoons O}$ from experimentally measurable affinities. K_d^{ens} and K_d^C were experimentally measured here (Figure S3). K_d^O for cRGD or Fn in the

presence of Mn^{2+} was difficult to measure accurately by fluorescence polarization because ligand binding/dissociation rates for the open conformation were too slow for the system to reach equilibrium. Instead, we estimated K_d^O based on our previous affinity measurements for α5β1 (8,16), which found that K_d^O was ~2000–7000 times smaller than K_d^C (Table S2).

Eqs.5–6 are according to the law of conservation of mass. When known concentrations of α5β1 headpiece and ligand are mixed, the equilibrium concentrations of each species ([C], [O], [L], [C·L] and [O·L]) can be solved simultaneously using numeric methods from Eqs.2–6 in which K_d^C, K_d^O, K_d^{ens}, $[\alpha5\beta1]_{total}$ and $[L]_{total}$ were known inputs. The percentage of ligand-bound α5β1 headpiece was then calculated by Eq.7. The percentages of closed and open complexes were calculated by Eqs.8–9, respectively. The results were listed in Table S3.

Acknowledgements
This work was supported by NIH grant R01-HL-131729 and a research collaboration with Waters Corporation (JRE).

Conflict of Interest
The Authors declare that they have no conflicts of interest with the contents of this article.

Data Availability
All manuscript data can be found in the main text, figures, and supplemental files. The raw HDX MS data have been deposited to the ProteomeXchange Consortium via the PRIDE partner repository with the dataset identifier PXD031508.

Author Contributions
Y.S.: investigation, formal analysis, visualization, writing – original draft, writing – review & editing; R.E.I.: investigation, formal analysis, writing – review and editing; J.L.: formal analysis; J.R.E.: formal analysis, methodology, resources, writing – review & editing; T.A.S.: conceptualization, formal analysis, funding acquisition, project administration, supervision, writing – review & editing.

Description of Supplemental Files
This article contains supporting information (8,16,44,45).
Supplemental Figures S1-S9
Supplemental Tables S1-S3
Supplemental Datafile containing expanded HDX MS experimental details and parameters, as well as the measured relative deuterium levels and percent deuteration values for all peptides described in both figures and text.

Figure Legends

Figure 1. α5β1 and fibronectin structures. (A) Three overall conformations of α5β1. (B) Representative negative stain EM class averages for each conformation of α5β1; the EO conformation is bound to Fn7–10. Scale bars are 10 nm. From (6). (C-D) Structures of α5β1 headpiece alone (PDB 3VI3)(C) and in complex with Fn7–10 (PDB 7NWL)(D). (E) Close-up view of the α5β1/Fn7–10 interface.

Figure 2. Hydrogen-deuterium exchange of Fn9–10 and Fn7–10. (A-D) HDX of Fn9–10 and Fn7–10 fragments in the absence of α5β1 is color coded for all peptides on the sequence (A-B) or on the structures (C-D) at all time points. (A-B) show all overlapping peptides at each time point, with each row showing a different set of non-overlapping peptides. The percent deuterated values of each colored peptide are provided in Supplementary Figure S3 and in the Supplementary Datafile. (C-D) Ribbon cartoons (PDB code 1FNF) color-coded for each overlapping peptide; regions not covered by HDX are shown in black dotted lines. All peptides are shown in this representation by dividing the ribbon representation into different segments for each overlapping peptide. (E-G) Deuterium uptake curves for selected peptides.

Figure 3. Stabilities and binding affinities of Fn fragments. (A) Thermal unfolding of Fn fragments monitored by tryptophan fluorescence. (B) Chemical unfolding of Fn fragments monitored by tryptophan fluorescence. Data for Fn9–10, Fn^{R}9–10 and Fn^{RPR}9–10 were fit with shared m (fitting result $m = 1.25 \pm 0.02$ kcal·L·mol^{-2}). (C-D) Affinities measured in triplicate by fluorescence polarization with 100 nM α5β1 headpiece or α5β1 ectodomain, 10 nM FITC-cRGD probe, and competition with varying concentrations of Fn9–10 or Fn7–10 in the presence of 1 mM Ca^{2+}/Mg^{2}. (C) Representative competitive binding curves; all conditions are shown in supplementary Figure S2. (D) shows K_d values with fitting errors.

Figure 4. Alteration in Fn HDX upon binding of α5β1. (A) Differences in HDX of Fn9–10 and Fn7–10 with and without α5β1-bound ($\Delta D = D_{\text{bound Fn}} - D_{\text{free Fn}}$) are shown for each peptide plotted at the midpoint of its sequence position. The difference calculation was performed using the data shown in Supplemental Figures S1 and S4, for free and bound forms, respectively. All deuteration values and peptide sequences are found in the Supplementary Datafile. Horizontal dashed lines mark $\Delta D = 0, \pm 0.7$ Da. For interpreting the HDX difference data we chose a difference of 0.7 Da to mark differences that are clearly above the error of measurement and are likely meaningful. (B-D) Deuterium uptake curves for selected peptides.

Figure 5. HDX of α5β1 headpiece in ligand-free (A), cRGD-bound (B), Fn9–10-bound (C) and Fn7–10-bound (D) states at 4 hr are shown on the structure (PDB 3VI3) as ribbon cartoons, color coded according to the key. Regions not covered by HDX are shown in black dotted lines. All structures are shown in the closed conformation for comparison regardless of the actual conformations of the α5β1 headpiece in each state. All peptides are shown in this representation by dividing the ribbon representation into different segments for each overlapping peptide. The percent deuterated values of each colored peptide are provided in Supplementary Figures S5-8 and in the Supplementary Datafile.

Figure 6. Deuterium uptake curves for selected peptides of α5β1 headpiece in absence of ligand and presence of cRGD, Fn9–10, and Fn7–10. All deuteration values are found in the Supplementary Datafile.

Figure 7. Deuterium uptake differences between ligand-bound and free α5β1 headpiece. (A, B) Deuterium uptake differences between Fn7–10-bound and free α5β1 headpiece ($\Delta D = D_{\alpha5\beta1\cdot Fn7–10} - D_{\text{free } \alpha5\beta1}$) are shown on the closed (A) and open (B) α5β1 headpiece structures (3VI4 and 7NWL, respectively) for comparison. Peptides are colored as shown in the key by their ΔD at following time points: β-ribbon, SDL2 and C-D loops at 10 s; α1 and α1′ helices at 10 m; F-G (α5 subunit), SDL3, α3-β4, α5-β5 and F-G (β1 subunit) loops and α2 and α7 helices at 1 hr; W2β4-W3β1 loop at 4 hr. Regions not covered by HDX are shown in black dotted lines. (C, D) $\Delta D = D_{\text{ligand bound-}\alpha5\beta1} - D_{\text{free } \alpha5\beta1}$ for each peptide is plotted at the midpoint of its sequence position. Horizontal dashed lines mark ΔD = 0, ±0.7 Da, as described in Figure 4. The difference calculation was performed using the data shown in Supplemental Figure S5-S8, for free and bound forms, respectively. All deuteration values and peptide sequences are found in the Supplementary Datafile.

References

1. Singh, P., Carraher, C., and Schwarzbauer, J. E. (2010) Assembly of fibronectin extracellular matrix. *Annu Rev Cell Dev Biol* **26**, 397-419

2. Schwarzbauer, J. E., and DeSimone, D. W. (2011) Fibronectins, their fibrillogenesis, and in vivo functions. *Cold Spring Harb Perspect Biol* **3**, 1-19

3. Goh, K. L., Yang, J. T., and Hynes, R. O. (1997) Mesodermal defects and cranial neural crest apoptosis in α5 integrin-null embryos. *Development* **124**, 4309-4319

4. Francis, S. E., Goh, K. L., Hodivala-Dilke, K., Bader, B. L., Stark, M., Davidson, D., and Hynes, R. O. (2002) Central roles of α5β1 integrin and fibronectin in vascular development in mouse embryos and embryoid bodies. *Arterioscler Thromb Vasc Biol* **22**, 927-933

5. Schaffner, F., Ray, A. M., and Dontenwill, M. (2013) Integrin α5β1, the fibronectin receptor, as a pertinent therapeutic target in solid tumors. *Cancers (Basel)* **5**, 27-47

6. Su, Y., Xia, W., Li, J., Walz, T., Humphries, M. J., Vestweber, D., Cabañas, C., Lu, C., and Springer, T. A. (2016) Relating conformation to function in integrin α5β1. *Proc Natl Acad Sci U S A.* **113**, E3872-3881

7. Miyazaki, N., Iwasaki, K., and Takagi, J. (2018) A systematic survey of conformational states in β1 and β4 integrins using negative-stain electron microscopy. *J Cell Sci* **131**

8. Li, J., Su, Y., Xia, W., Qin, Y., Humphries, M. J., Vestweber, D., Cabanas, C., Lu, C., and Springer, T. A. (2017) Conformational equilibria and intrinsic affinities define integrin activation. *EMBO J* **36**, 629-645

9. Springer, T. A., and Dustin, M. L. (2012) Integrin inside-out signaling and the immunological synapse. *Curr. Opin. Cell Biol.* **24**, 107-115

10. Zhu, J., Luo, B. H., Barth, P., Schonbrun, J., Baker, D., and Springer, T. A. (2009) The structure of a receptor with two associating transmembrane domains on the cell surface: Integrin αIIbβ3. *Mol. Cell* **34**, 234-249

11. Lau, T. L., Kim, C., Ginsberg, M. H., and Ulmer, T. S. (2009) The structure of the integrin αIIbβ3 transmembrane complex explains integrin transmembrane signalling. *EMBO J* **9**, 1351-1361

12. Schumacher, S., Dedden, D., Nunez, R. V., Matoba, K., Takagi, J., Biertumpfel, C., and Mizuno, N. (2021) Structural insights into integrin α5β1 opening by fibronectin ligand. *Sci Adv* **7**, eabe9716

13. Nagae, M., Re, S., Mihara, E., Nogi, T., Sugita, Y., and Takagi, J. (2012) Crystal structure of α5β1 integrin ectodomain: Atomic details of the fibronectin receptor. *J Cell Biol* **197**, 131-140

14. Xia, W., and Springer, T. A. (2014) Metal ion and ligand binding of integrin α5β1. *Proc. Natl. Acad. Sci. U. S. A.* **111**, 17863-17868

15. Zhu, J., Zhu, J., and Springer, T. A. (2013) Complete integrin headpiece opening in eight steps. *J. Cell Biol.* **201**, 1053-1068

16. Anderson, J. M., Li, J., and Springer, T. A. (2022) Regulation of integrin α5β1 conformational states and intrinsic affinities by metal ions and the ADMIDAS. *Mol Biol Cell* **33**, ar56

17. Takagi, J., Strokovich, K., Springer, T. A., and Walz, T. (2003) Structure of integrin α5β1 in complex with fibronectin. *EMBO J* **22**, 4607-4615

18. Obara, M., Kang, M. S., and Yamada, K. M. (1988) Site-directed mutagenesis of the cell-binding domain of human fibronectin: separable, synergistic sites mediate adhesive function. *Cell* **53**, 649-657

19. Aota, S., Nomizu, M., and Yamada, K. M. (1994) The short amino acid sequence Pro-His-Ser-Arg-Asn in human fibronectin enhances cell-adhesive function. *J Biol Chem* **269**, 24756-24761

20. Mould, A. P., Askari, J. A., Aota, S., Yamada, K. M., Irie, A., Takada, Y., Mardon, H. J., and Humphries, M. J. (1997) Defining the topology of integrin α5β1-fibronectin interactions using inhibitory anti-α5 and anti-β1 monoclonal antibodies. Evidence that the synergy sequence of fibronectin is recognized by the amino-terminal repeats of the α5 subunit. *J Biol Chem* **272**, 17283-17292

21. Redick, S. D., Settles, D. L., Briscoe, G., and Erickson, H. P. (2000) Defining fibronectin's cell adhesion synergy site by site-directed mutagenesis. *J Cell Biol* **149**, 521-527

22. Altroff, H., Choulier, L., and Mardon, H. J. (2003) Synergistic activity of the ninth and tenth FIII domains of human fibronectin depends upon structural stability. *J Biol Chem* **278**, 491-497

23. Wales, T. E., and Engen, J. R. (2006) Hydrogen exchange mass spectrometry for the analysis of protein dynamics. *Mass Spectrometry Reviews* **25**, 158-170

24. Main, A. L., Harvey, T. S., Baron, M., Boyd, J., and Campbell, I. D. (1992) The three-dimensional structure of the tenth type III module of fibronectin: an insight into RGD-mediated interactions. *Cell* **71**, 671-678

25. Copie, V., Tomita, Y., Akiyama, S. K., Aota, S., Yamada, K. M., Venable, R. M., Pastor, R. W., Krueger, S., and Torchia, D. A. (1998) Solution structure and dynamics of linked cell attachment modules of mouse fibronectin containing the RGD and synergy regions: comparison with the human fibronectin crystal structure. *J. Mol. Biol.* **277**, 663-682

26. Litvinovich, S. V., and Ingham, K. C. (1995) Interactions between type III domains in the 110 kDa cell-binding fragment of fibronectin. *J Mol Biol* **248**, 611-626

27. Plaxco, K. W., Spitzfaden, C., Campbell, I. D., and Dobson, C. M. (1997) A comparison of the folding kinetics and thermodynamics of two homologous fibronectin type III modules. *J Mol Biol* **270**, 763-770

28. Koivunen, E., Wang, B., and Ruoslahti, E. (1995) Phage libraries displaying cyclic peptides with different ring sizes: ligand specificities of the RGD-directed integrins. *Biotechnology (N Y)* **13**, 265-270

29. Humphries, J. D., Askari, J. A., Zhang, X. P., Takada, Y., Humphries, M. J., and Mould, A. P. (2000) Molecular basis of ligand recognition by integrin α5β1: II. Specificity of Arg-Gly-Asp binding is determined by Trp157 of the α subunit. *J. Biol. Chem.* **275**, 20337-20345

30. Li, J., and Springer, T. A. (2018) Energy landscape differences among integrins establish the framework for understanding activation. *J Cell Biol* **217**, 397-412

31. Weis, D. D., Wales, T. E., Engen, J. R., Hotchko, M., and Ten Eyck, L. F. (2006) Identification and characterization of EX1 kinetics in H/D exchange mass spectrometry by peak width analysis. *J Am Soc Mass Spectrom* **17**, 1498-1509

32. Xiao, T., Takagi, J., Wang, J.-H., Coller, B. S., and Springer, T. A. (2004) Structural basis for allostery in integrins and binding of fibrinogen-mimetic therapeutics. *Nature* **432**, 59-67

33. Sen, M., Yuki, K., and Springer, T. A. (2013) An internal ligand-bound, metastable state of a leukocyte integrin, $\alpha_X\beta_2$. *J. Cell Biol.* **203**, 629-642

34. Ruoslahti, E., and Pierschbacher, M. D. (1986) Arg-Gly-Asp: A versatile cell recognition signal. *Cell* **44**, 517-518

35. Springer, T. A. (1997) Folding of the N-terminal, ligand-binding region of integrin α-subunits into a β-propeller domain. *Proc. Natl. Acad. Sci. U. S. A.* **94**, 65-72

36. Suel, G. M., Lockless, S. W., Wall, M. A., and Ranganathan, R. (2003) Evolutionarily conserved networks of residues mediate allosteric communication in proteins. *Nat. Struct. Biol.* **10**, 59-69

37. Takagi, J., Erickson, H. P., and Springer, T. A. (2001) C-terminal opening mimics "inside-out" activation of integrin $\alpha_5\beta_1$. *Nat. Struct. Biol.* **8**, 412-416

38. Santoro, M. M., and Bolen, D. W. (1988) Unfolding free energy changes determined by the linear extrapolation method. 1. Unfolding of phenylmethanesulfonyl alpha-chymotrypsin using different denaturants. *Biochemistry* **27**, 8063-8068

39. Myers, J. K., Pace, C. N., and Scholtz, J. M. (1995) Denaturant m values and heat capacity changes: relation to changes in accessible surface areas of protein unfolding. *Protein Sci* **4**, 2138-2148

40. Wang, J., Su, Y., Iacob, R. E., Engen, J. R., and Springer, T. A. (2019) General structural features that regulate integrin affinity revealed by atypical αVβ8. *Nat Commun* **10**, 5481

41. Masson, G. R., Burke, J. E., Ahn, N. G., Anand, G. S., Borchers, C., Brier, S., Bou-Assaf, G. M., Engen, J. R., Englander, S. W., Faber, J., Garlish, R., Griffin, P. R., Gross, M. L., Guttman, M., Hamuro, Y., Heck, A. J. R., Houde, D., Iacob, R. E., Jorgensen, T. J. D., Kaltashov, I. A., Klinman, J. P., Konermann, L., Man, P., Mayne, L., Pascal, B. D., Reichmann, D., Skehel, M., Snijder, J., Strutzenberg, T. S., Underbakke, E. S., Wagner, C., Wales, T. E., Walters, B. T., Weis, D. D., Wilson, D. J., Wintrode, P. L., Zhang, Z., Zheng, J., Schriemer, D. C., and Rand, K. D. (2019) Recommendations for performing, interpreting and reporting hydrogen deuterium exchange mass spectrometry (HDX-MS) experiments. *Nat Methods* **16**, 595-602

42. Perez-Riverol, Y., Bai, J., Bandla, C., Garcia-Seisdedos, D., Hewapathirana, S., Kamatchinathan, S., Kundu, D. J., Prakash, A., Frericks-Zipper, A., Eisenacher, M., Walzer, M., Wang, S., Brazma, A., and Vizcaino, J. A. (2022) The PRIDE database resources in 2022: a hub for mass spectrometry-based proteomics evidences. *Nucleic Acids Res* **50**, D543-D552

43. Wales, T. E. F., K. E.; Gerhardt, G. C.; Engen, J. R. (2008) High-speed and high-resolution UPLC separation at zero degrees Celsius. *Anal Chem* **80**, 6815-6820

44. Houde, D. B., S.; A.; Engen, J. R. (2011) The utility of hydrogen/deuterium exchange mass spectrometry in biopharmaceutical comparability studies. *J Pharm Sci* **100**, 2071-2086

45. Engen, J. R., and Wales, T. E. (2015) Analytical Aspects of Hydrogen Exchange Mass Spectrometry. *Annu Rev Anal Chem (Palo Alto Calif)* **8**, 127-148

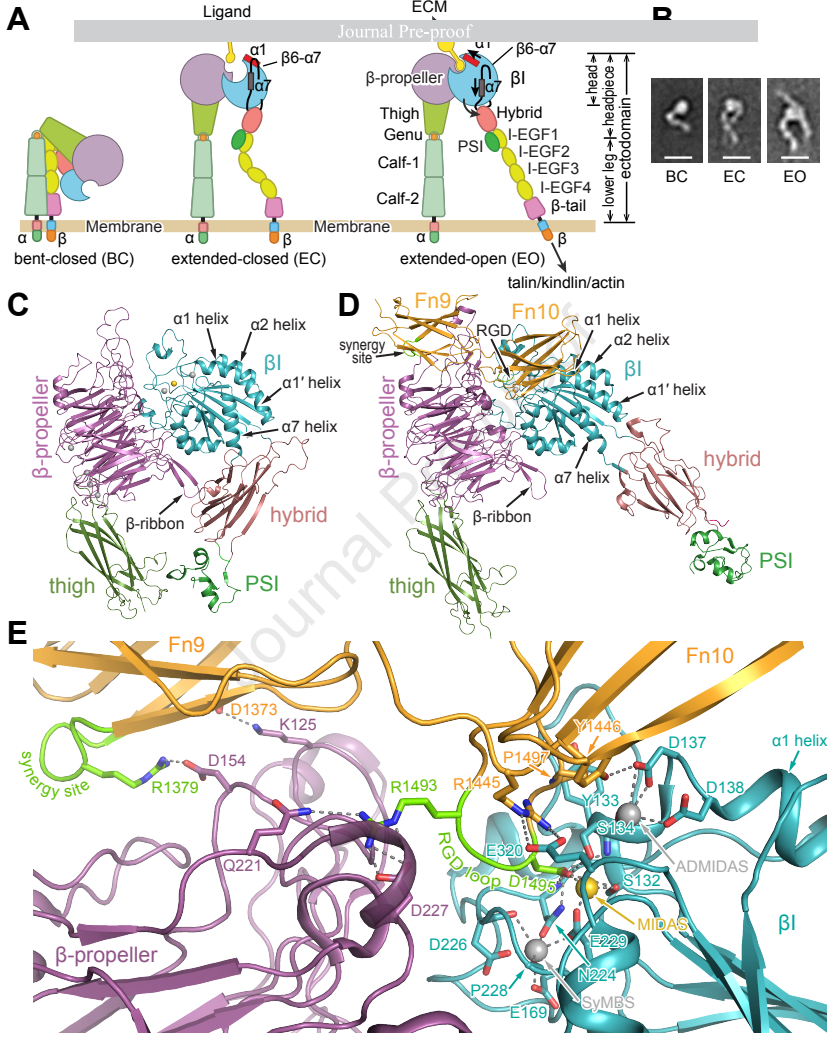
A
Ligand
ECM
Journal Pre-proof
α1
β6-α7
α7
β-propeller
βI
Thigh
Genu
Calf-1
Calf-2
Hybrid
PSI
I-EGF1
I-EGF2
I-EGF3
I-EGF4
β-tail
head
headpiece
lower leg
ectodomain
Membrane
α
β
bent-closed (BC)
extended-closed (EC)
extended-open (EO)
talin/kindlin/actin
B
BC
EC
EO
C
α1 helix
α2 helix
βI
α1′ helix
α7 helix
β-propeller
β-ribbon
hybrid
thigh
PSI
D
Fn9
Fn10
synergy site
RGD
α1 helix
α2 helix
βI
α1′ helix
β-propeller
α7 helix
hybrid
β-ribbon
PSI
thigh
E
Fn9
Fn10
D1373
K125
synergy site
D154
R1379
R1493
R1445
Y1446
P1497
D137
α1 helix
D138
Y133
S134
S132
ADMIDAS
E320
RGD loop
D1495
Q221
D227
MIDAS
D226
E229
N224
P228
SyMBS
E169
β-propeller
βI

Figure 1

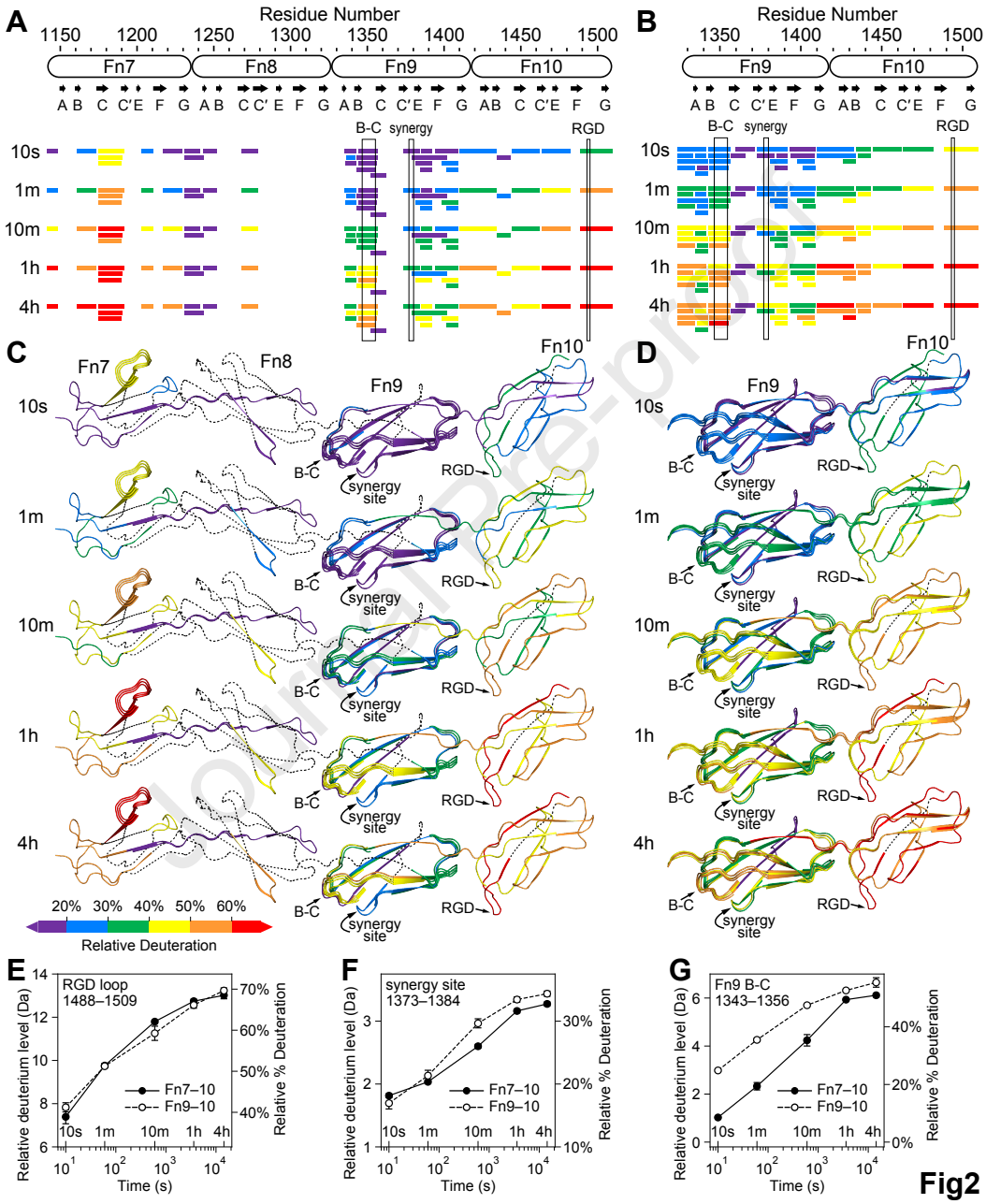

Fig2

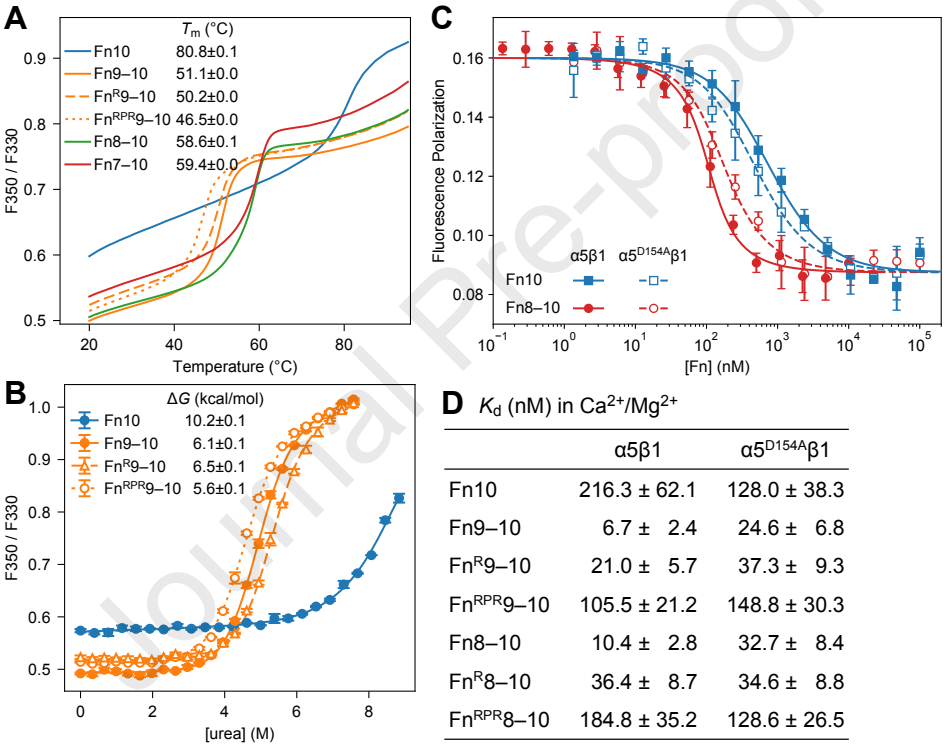

D K_d (nM) in Ca^{2+}/Mg^{2+}

	α5β1	α5^{D154A}β1
Fn10	216.3 ± 62.1	128.0 ± 38.3
Fn9–10	6.7 ± 2.4	24.6 ± 6.8
Fn^{R}9–10	21.0 ± 5.7	37.3 ± 9.3
Fn^{RPR}9–10	105.5 ± 21.2	148.8 ± 30.3
Fn8–10	10.4 ± 2.8	32.7 ± 8.4
Fn^{R}8–10	36.4 ± 8.7	34.6 ± 8.8
Fn^{RPR}8–10	184.8 ± 35.2	128.6 ± 26.5

Figure 3

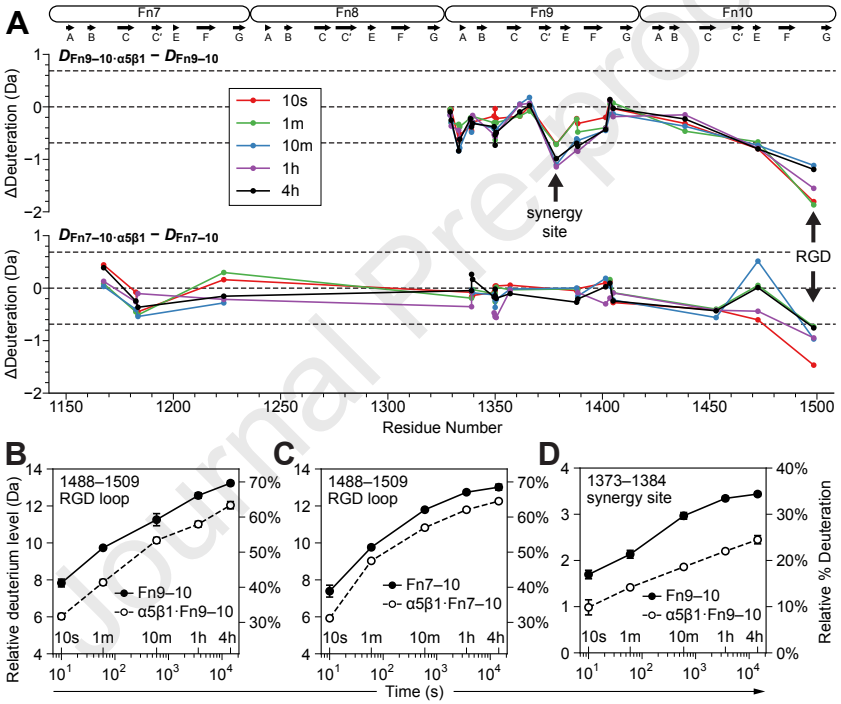

Figure 4

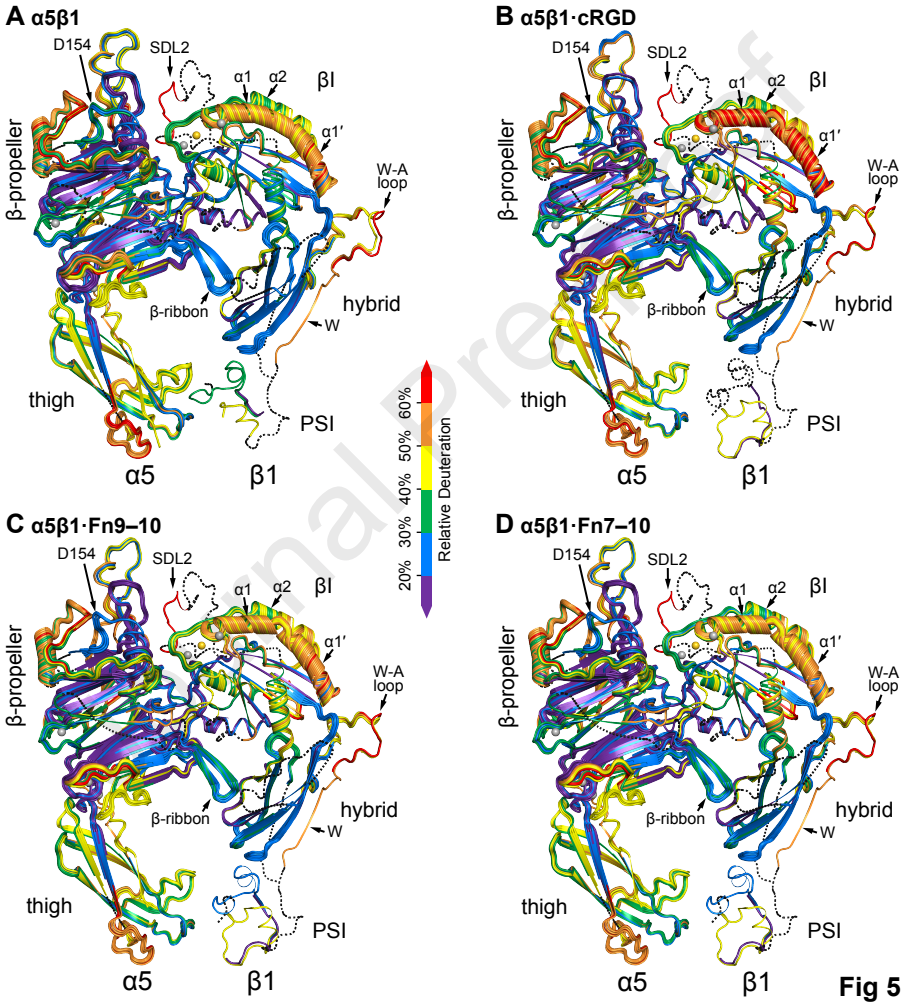

Fig 5

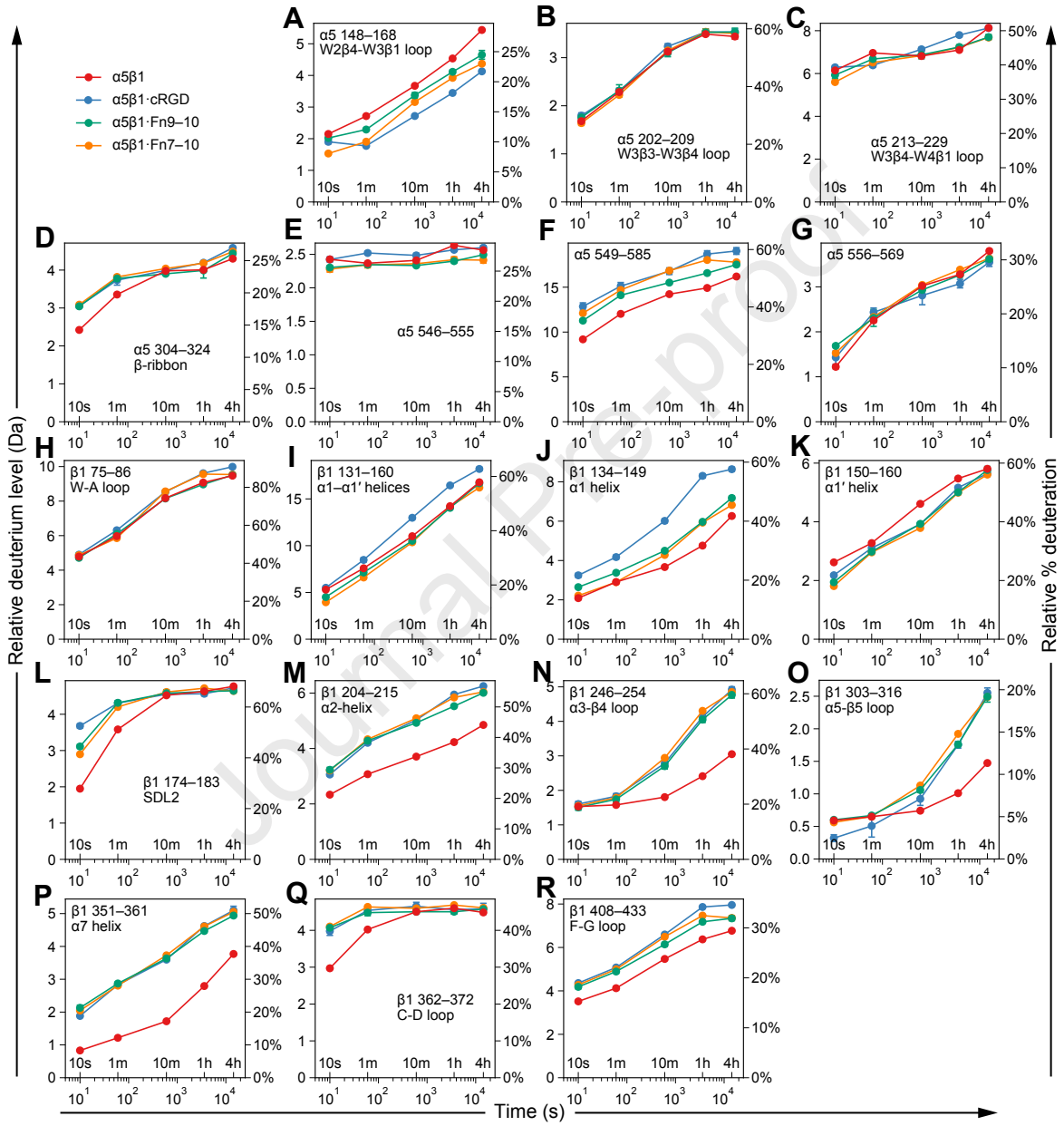
α5β1
α5β1·cRGD
α5β1·Fn9–10
α5β1·Fn7–10
A α5 148–168 W2β4-W3β1 loop
B α5 202–209 W3β3-W3β4 loop
C α5 213–229 W3β4-W4β1 loop
D α5 304–324 β-ribbon
E α5 546–555
F α5 549–585
G α5 556–569
H β1 75–86 W-A loop
I β1 131–160 α1–α1′ helices
J β1 134–149 α1 helix
K β1 150–160 α1′ helix
L β1 174–183 SDL2
M β1 204–215 α2-helix
N β1 246–254 α3-β4 loop
O β1 303–316 α5-β5 loop
P β1 351–361 α7 helix
Q β1 362–372 C-D loop
R β1 408–433 F-G loop
10s 1m 10m 1h 4h
Relative deuterium level (Da)
Relative % deuteration
Time (s)

Figure 6

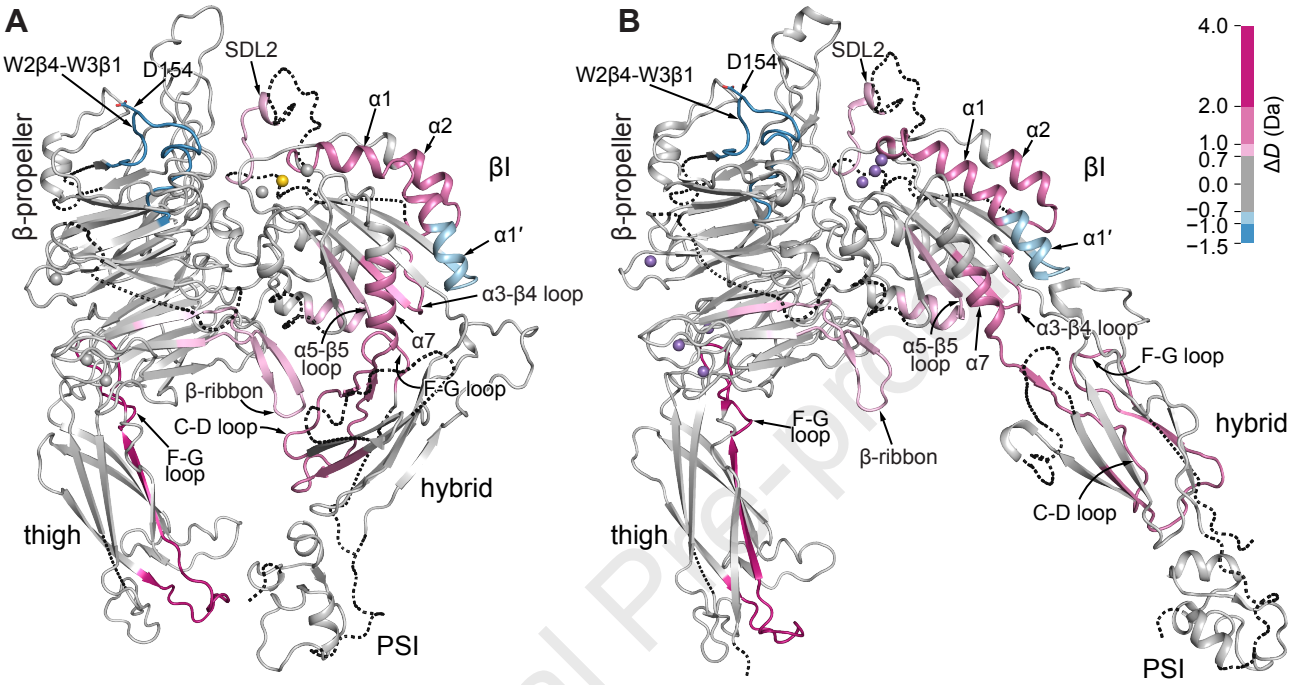

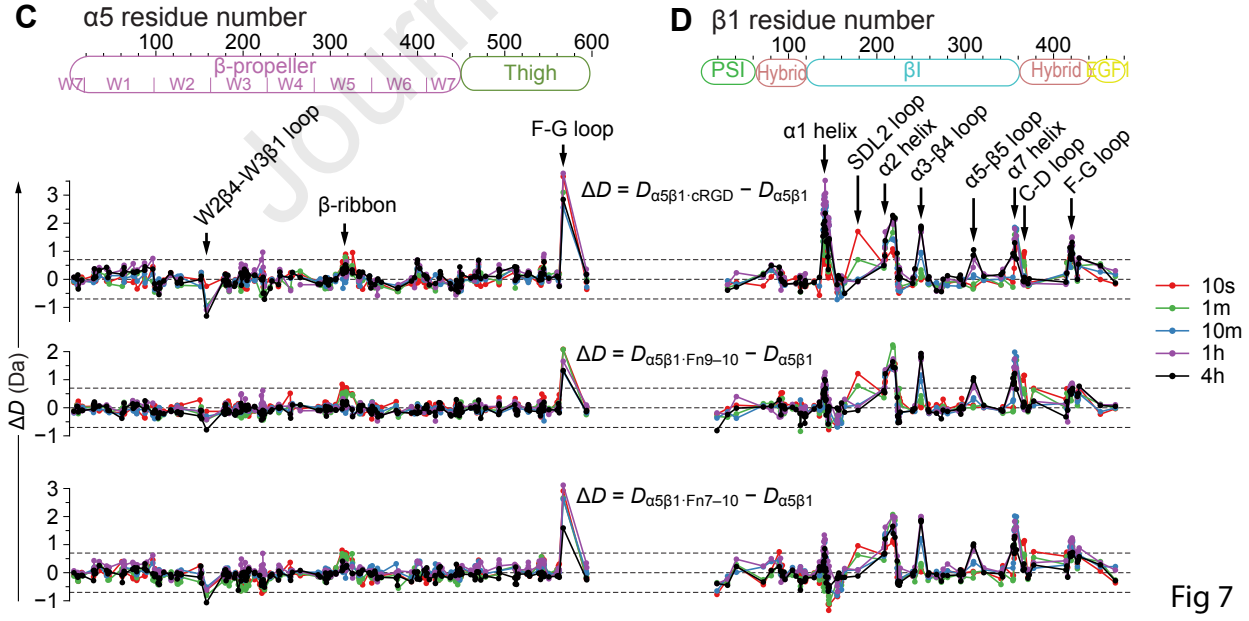

Fig 7

CRediT author statement

Yang Su: Investigation, Formal analysis, Visualization, Writing – original draft, Writing – review & editing **Roxana E. Iacob**: Investigation, Formal analysis, Writing – review and editing **Jing Li**: Formal analysis **John R. Engen**: Formal analysis, Methodology, Resources, Writing – review & editing **Timothy A. Springer**: Conceptualization, Formal analysis, Funding acquisition, Project administration, Supervision, Writing – review & editing

TABLE S1: HDX Data Summary and list of experimental parameters

DATASET	(1): Fn9–10	(2): Fn7–10	(3): α5β1	(4): α5β1 + cRGD	(5): α5β1 + Fn9–10	(6): α5β1 + Fn7–10
Sample buffer	20 mM Tris, 150 mM NaCl, 2 mM $MnCl_2$, 0.2 mM $CaCl_2$, H_2O, pH 7.4					
HDX reaction details[a]	Final D_2O concentration = 93.3%, pH_{read} = 7.0, 21 °C. See also footnote a					
HDX time course	10 s, 1 min, 10 min, 1 hr, 4 hr					
HDX controls	Minimum 3 undeuterated controls for each dataset					
Back-exchange	30–35%					
Number of peptides	30	32	α5=229 β1=113	α5=192 β1=102	α5=229 β1=113 Fn9–10=22	α5=229 β1=113 Fn7–10=20
Sequence coverage	97.3%	69.8%	α5=95.1% β1=83.8%	α5=94.7% β1=78.4%	α5=95.1% β1=83.8% Fn9–10=73.7%	α5=95.1% β1=83.8% Fn7–10=43.5%
Average peptide length	14	13.5	α5=15.7 β1=16.2	α5=16.0 β1=16.4	α5=15.7 β1=16.2 Fn9–10=12.9	α5=15.7 β1=16.2 Fn7–10=13.4
Redundancy	2.3	1.7	α5=6.2 β1=4.5	α5=5.3 β1=4.4	α5=6.2 β1=4.5 Fn9–10=2.1	α5=6.2 β1=4.5 Fn7–10=1.7
Replicates	2	2	1[b]	2[b]	4[b]	2[b]
Repeatability	±0.15 relative Da					
Meaningful differences[c]	> 0.70 Da					

[a] 15-fold dilution with labeling buffer (same as sample buffer except prepared with 99.9% D2O). 2-fold dilution with quench buffer [4 M GnHCl, 200 mM sodium phosphate, 0.5 M tris(2-carboxyethyl)phosphine hydrochloride (TCEP·HCl), H2O, pH2.5].

[b] total 9 replicates of α5β1. 7 replicates from datasets 3,5,6 used for peptide mapping.

[c] All reported values are the average relative deuterium level as given by the DynamX software, which in some cases is an average of more than one charge state, across all peptides in the replicates for each dataset. No statistical tests were applied to the HDX MS measurements. Rather, based on measurements of mean methodological error [+/- 0.14 Da (Houde D, Berkowitz SA, Engen JR. (2011). *J. Pharm. Sci.* 100(6), 2071-2086] we chose a value (+/- 0.35 Da) well above that as the threshold for calling differences in relative deuterium incorporation measurements meaningful. See also explanations of this methodology in Engen JR, Wales TE. (2015). *Annu. Rev. Anal. Chem.* 8, 127-148.

Table S2. Intrinsic affinities of the closed and open conformations for α5β1.

α5β1	Ligand	Metal Ions	K_d^C (nM)	K_d^O (nM)	K_d^C/K_d^O	Reference
Headpiece	cRGD	1 mM Ca^{2+}/ Mg^{2+}	8500±1400	1.9±0.3	4474	(1)
Unclasped ectodomain	cRGD	1 mM Ca^{2+}/Mg^{2+}	7000±3400	2.2±0.3	3182	(1)
Semi-truncated	cRGD	1 mM Ca^{2+}/Mg^{2+}	7100±900	2.1±0.4	3381	(1)
Unclasped ectodomain	Fn9–10	1 mM Ca^{2+}/Mg^{2+}	2900±1100	0.44±0.15	6591	(1)
Unclasped ectodomain	GRGDSPK	1 mM Ca^{2+}/Mg^{2+}	≥ 220000	71±5	≥ 3099	(2)
Unclasped ectodomain	GRGDSPK	2 mM Mn^{2+}	3300±130	1.6±0.2	2063	(2)
Unclasped ectodomain	cRGD	2 mM Mn^{2+}	46±5	—	—	(2)
Headpiece	cRGD	2 mM Mn^{2+}	46.2±0.3	—	—	This work

References

1. Li, J., Su, Y., Xia, W., Qin, Y., Humphries, M. J., Vestweber, D., Cabanas, C., Lu, C., and Springer, T. A. (2017) Conformational equilibria and intrinsic affinities define integrin activation, *EMBO J* **36**, 629-645. PMC5331762
2. Anderson, J. M., Li, J., and Springer, T. A. (2021) Regulation by metal ions and the ADMIDAS of integrin α5β1 conformational states and intrinsic affinities, *Preprint.*

Table S3. Conformational composition of free and ligand-bound α5β1 headpiece in the HDX samples.

Ligand	No Ligand	cRGD	Fn9–10	Fn7–10
K_d^{ens} (nM)		3.2±0.3[a]	0.41±0.24[b]	0.62±0.30[b]
K_d^C (nM)		43.9±3.2[a]	30.9±13.6[b]	27.7±14.8[b]
K_d^O (nM)[c]		0.022–0.0063	0.015–0.0044	0.014–0.0040
$[\alpha5\beta1]_{total}$ (μM)	74.5	59.6	47.3	54.4
$[Ligand]_{total}$ (μM)		119	47.3	54.4
% closed unliganded[c]	99.37–99.82	0.005–0.005	0.28–0.29	0.33–0.33
% open unliganded[c]	0.63–0.18	0.00–0.00	0.01–0.00	0.00–0.00
% bound α5β1[c]		99.99–99.99	99.71–99.71	99.66–99.66
% closed complex[c]		7.31–7.34	1.27–1.30	2.17–2.21
% open complex[c]		92.69–92.65	98.44–98.40	97.49–97.46

[a] Values are mean±standard deviation of three independent experiments.
[b] Errors are fitting errors.
[c] For values reported as a range, the first number was calculated by assuming $K_d^O = K_d^C / 2000$, and the second number was calculated by assuming $K_d^O = K_d^C / 7000$. α5β1's intrinsic affinity in the open conformation (K_d^O) was estimated to be 2000–7000-fold higher than in the closed conformation (K_d^C) based on previous affinity measurements of various α5β1 preparations as detailed in Table S2.

Figure S1. Complete HDX peptide coverage at each indicated time point for Fn9–10 and Fn7–10. Peptides are colored according to the key shown with relative deuteration (%) directly overlaid on each peptide.

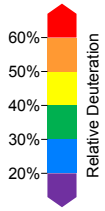

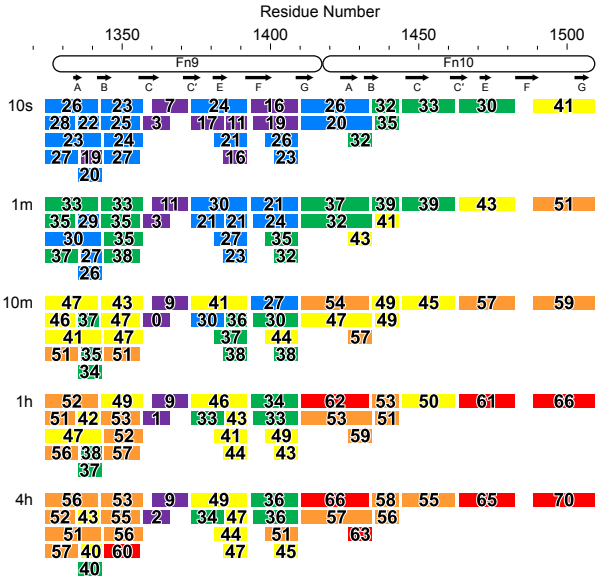

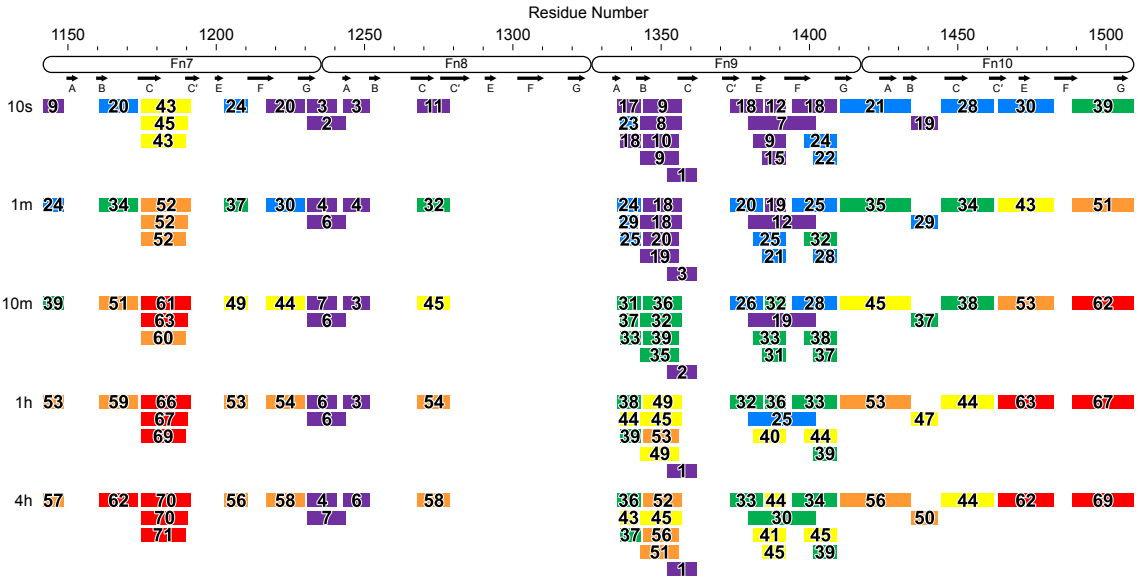

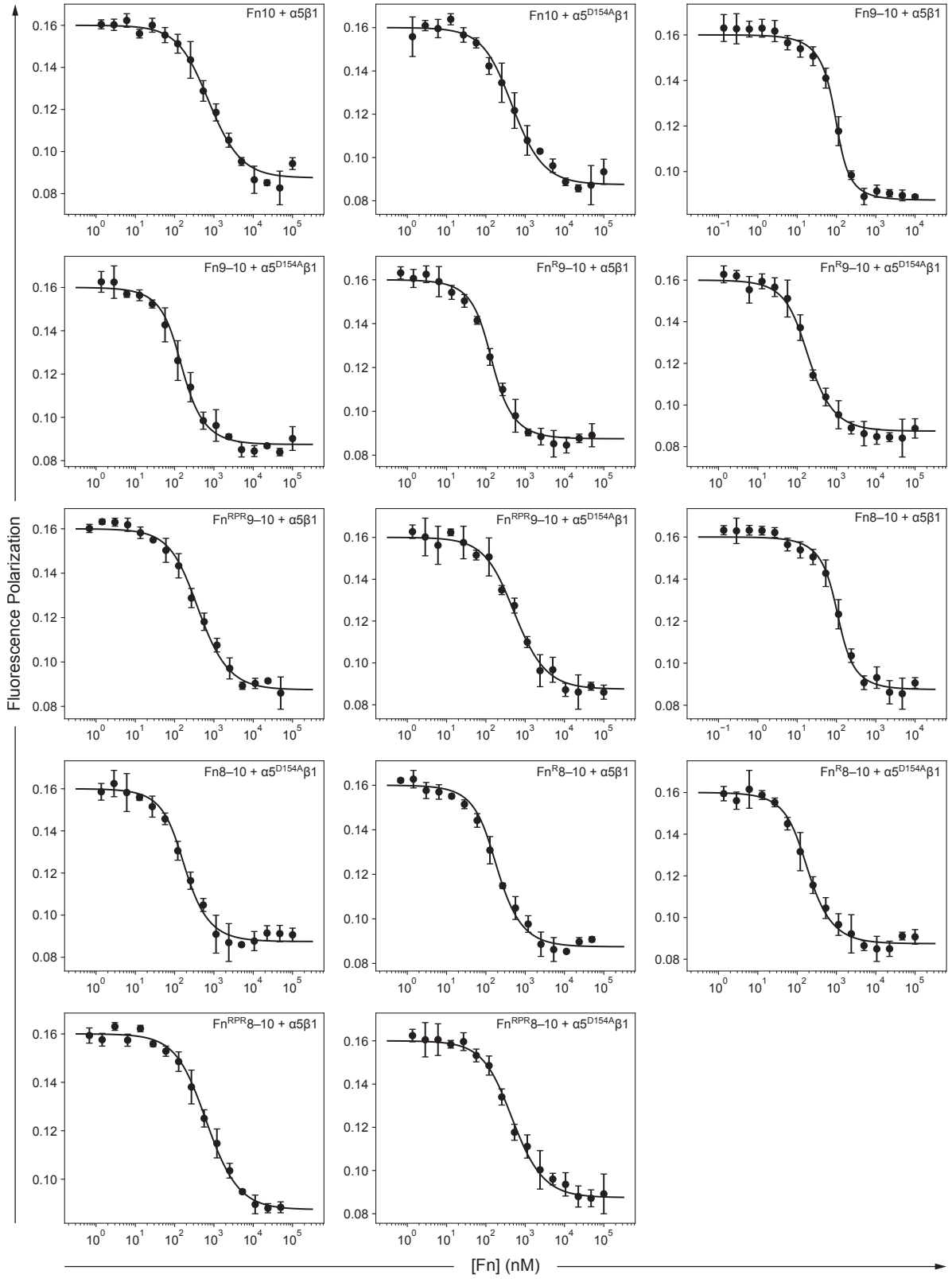

Figure S2. Affinities of α5β1 ectodomain for Fn fragments in the presence of Ca^{2+}/Mg^{2+}. Fitting results (K_d values) are listed in Figure 3D.

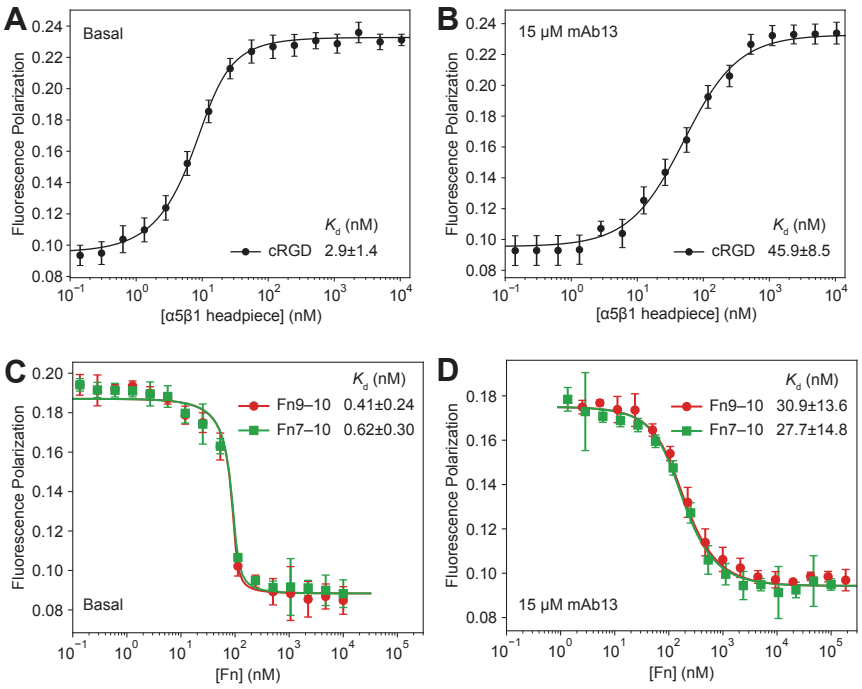

Figure S3. Affinities of α5β1 headpiece in the presence of Mn^{2+}. (A, B) Representative plots of basal ensemble affinity (A) and intrinsic affinity in the closed conformation (B) of α5β1 headpiece for cRGD. (C, D) Basal ensemble affinity (C) and intrinsic affinity in the closed conformation (D) of α5β1 headpiece for Fn9–10 and Fn7–10. In (B, D) the titrations were performed in the presence of 15 μM mAb13 Fab to saturably stabilize the closed conformation of α5β1 headpiece. Errors in K_d are fitting errors.

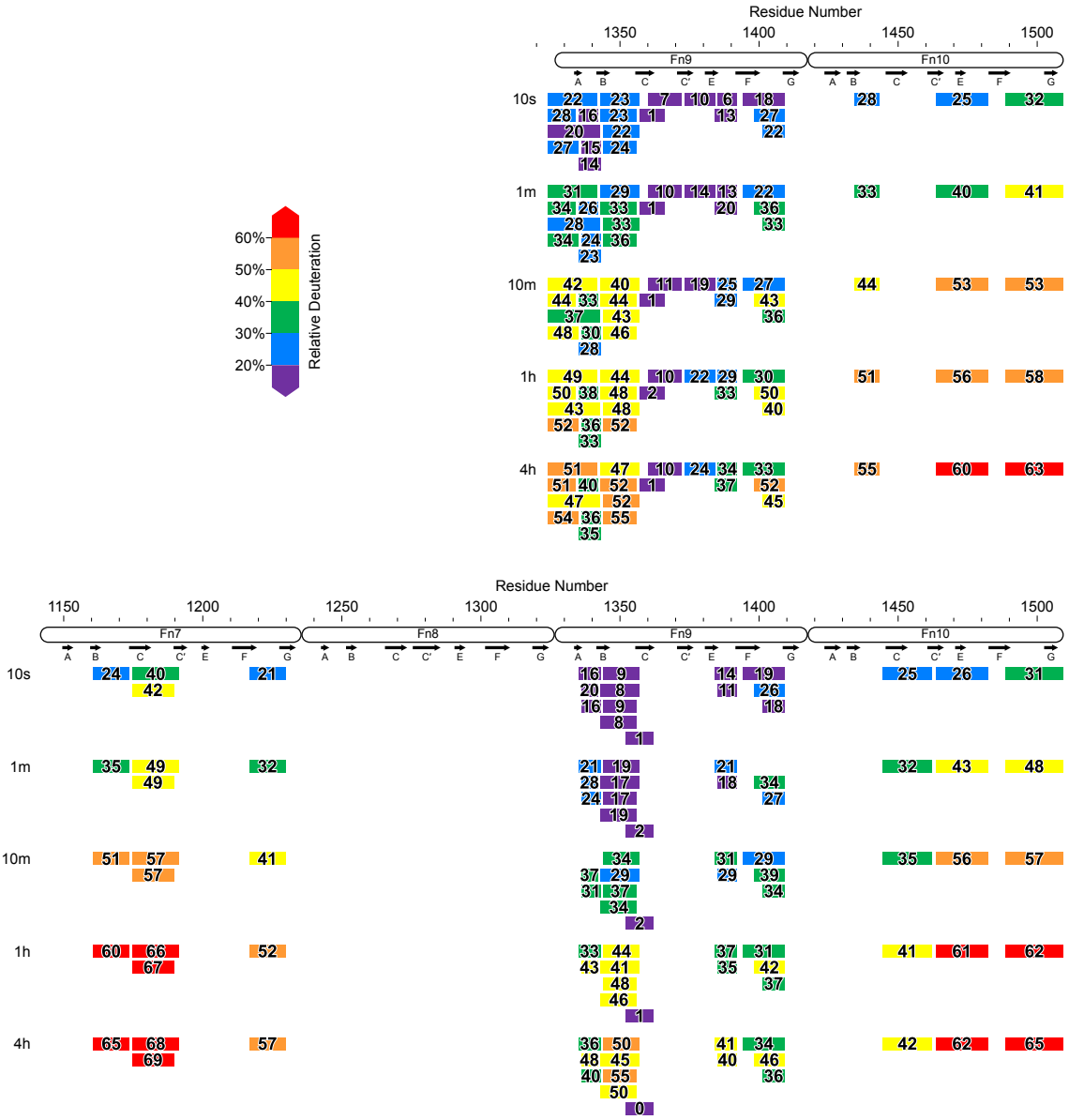

Figure S4. Complete HDX peptide coverage at each indicated time point for α5β1-bound Fn9–10 and Fn7–10. Peptides are colored according to the key shown with relative deuteration (%) directly overlaid on each peptide.

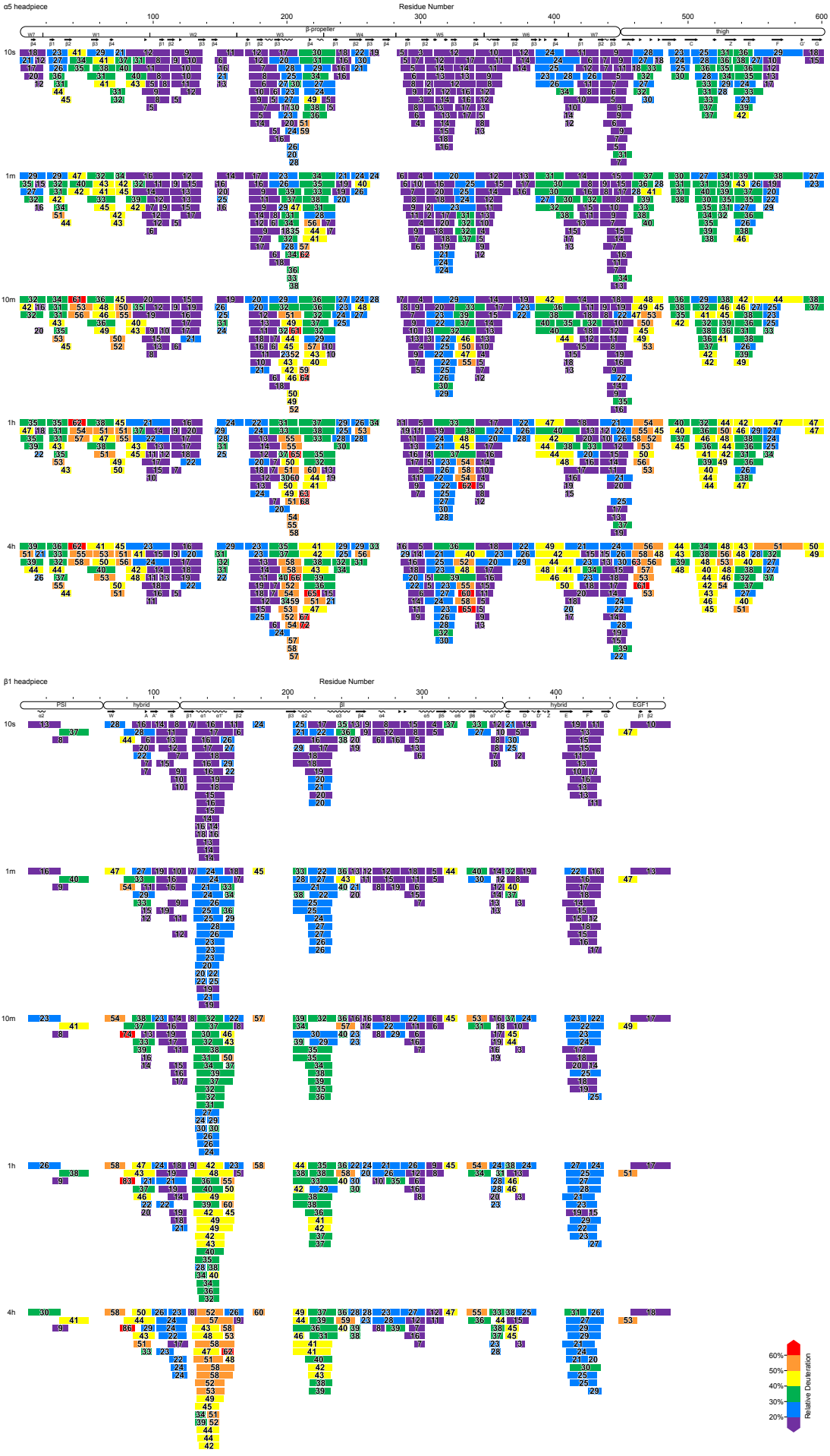

Figure S5. Complete HDX peptide coverage at each indicated time point for α5β1 headpiece. Peptides are colored according to the key shown with relative deuteration (%) directly overlaid on each peptide.

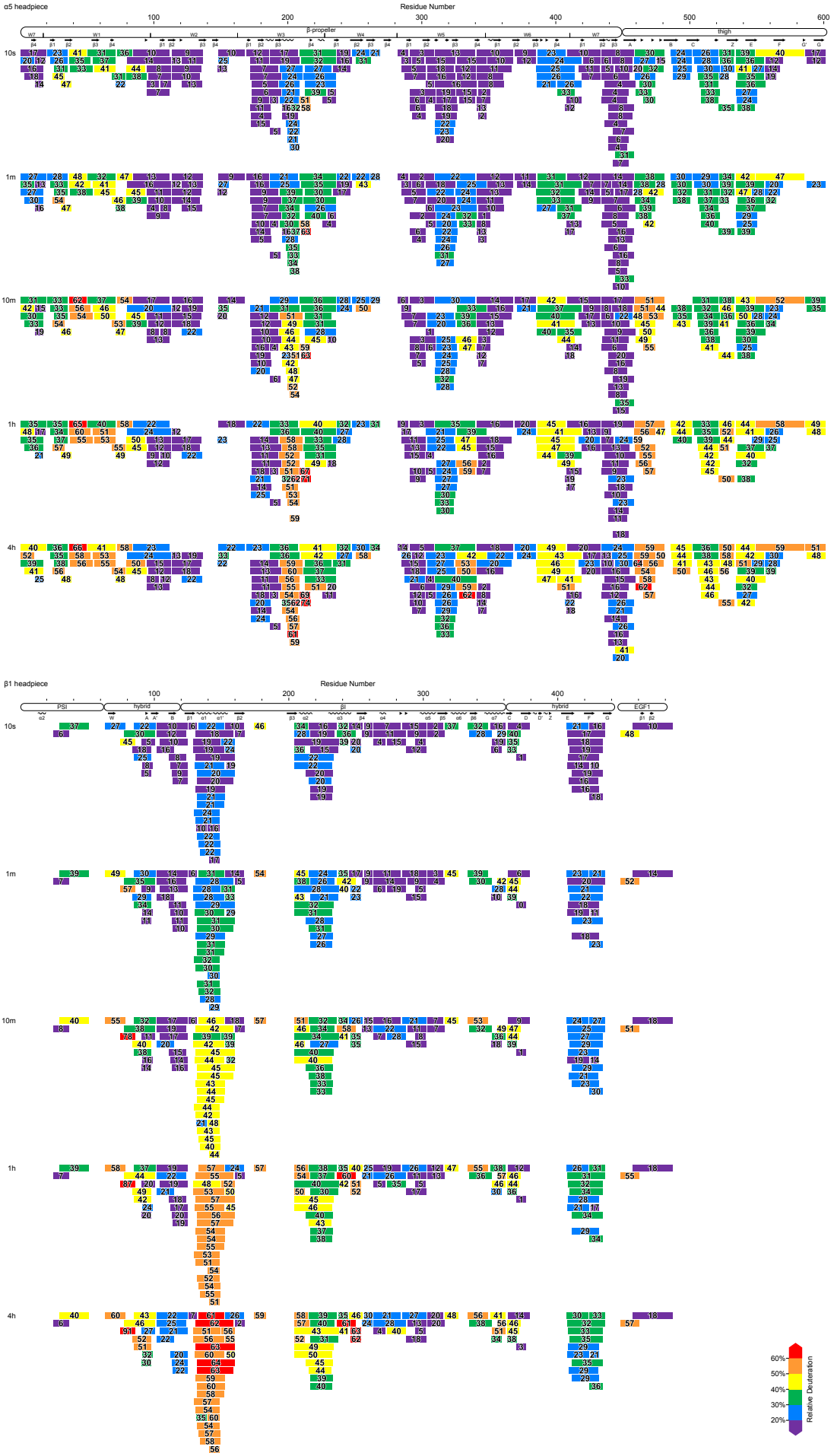

Figure S6. Complete HDX peptide coverage at each indicated time point for cRGD-bound α5β1 headpiece. Peptides are colored according to the key shown with relative deuteration (%) directly overlaid on each peptide.

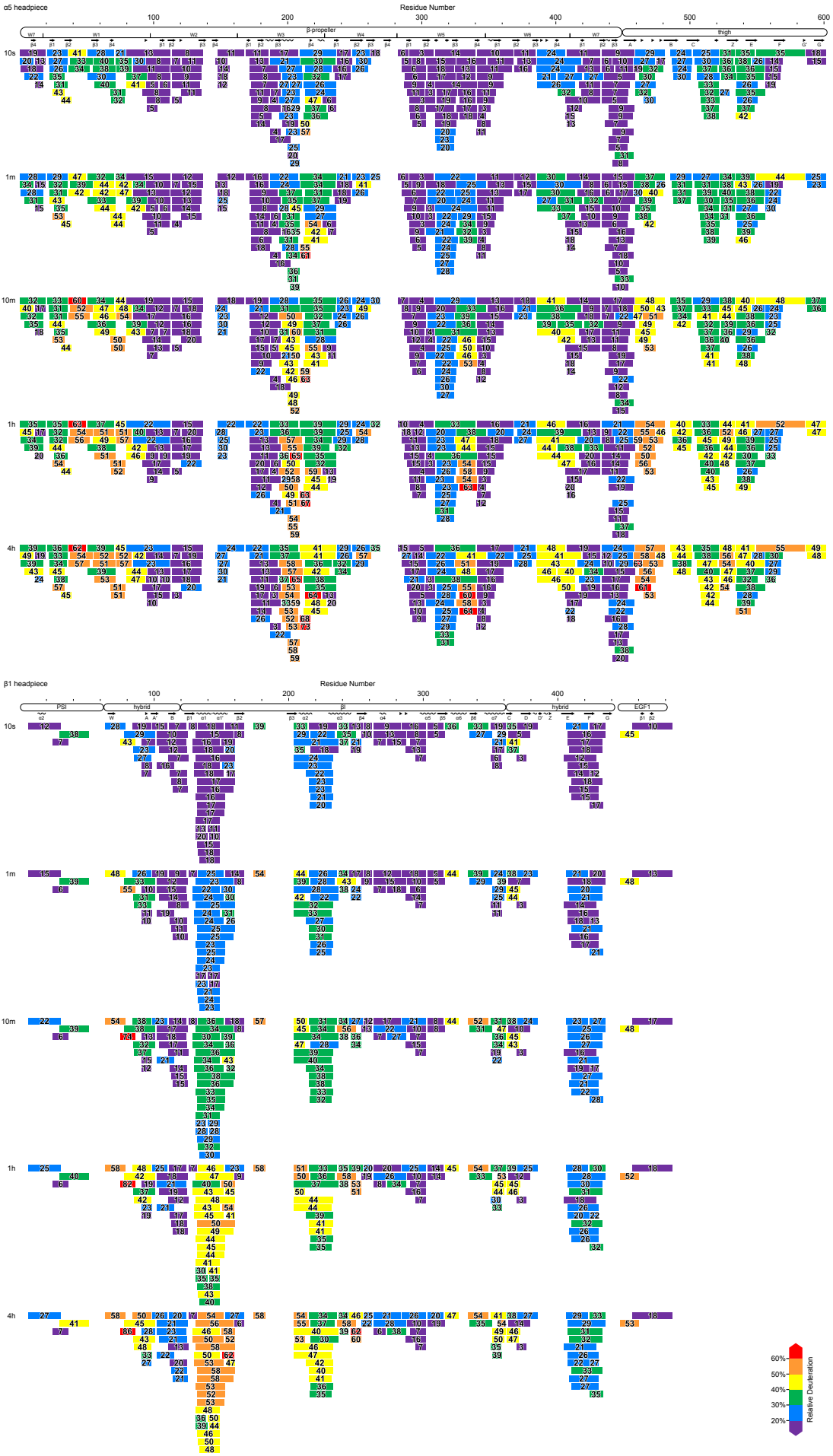

Figure S7. Complete HDX peptide coverage at each indicated time point for Fn9–10-bound α5β1 headpiece. Peptides are colored according to the key shown with relative deuteration (%) directly overlaid on each peptide.

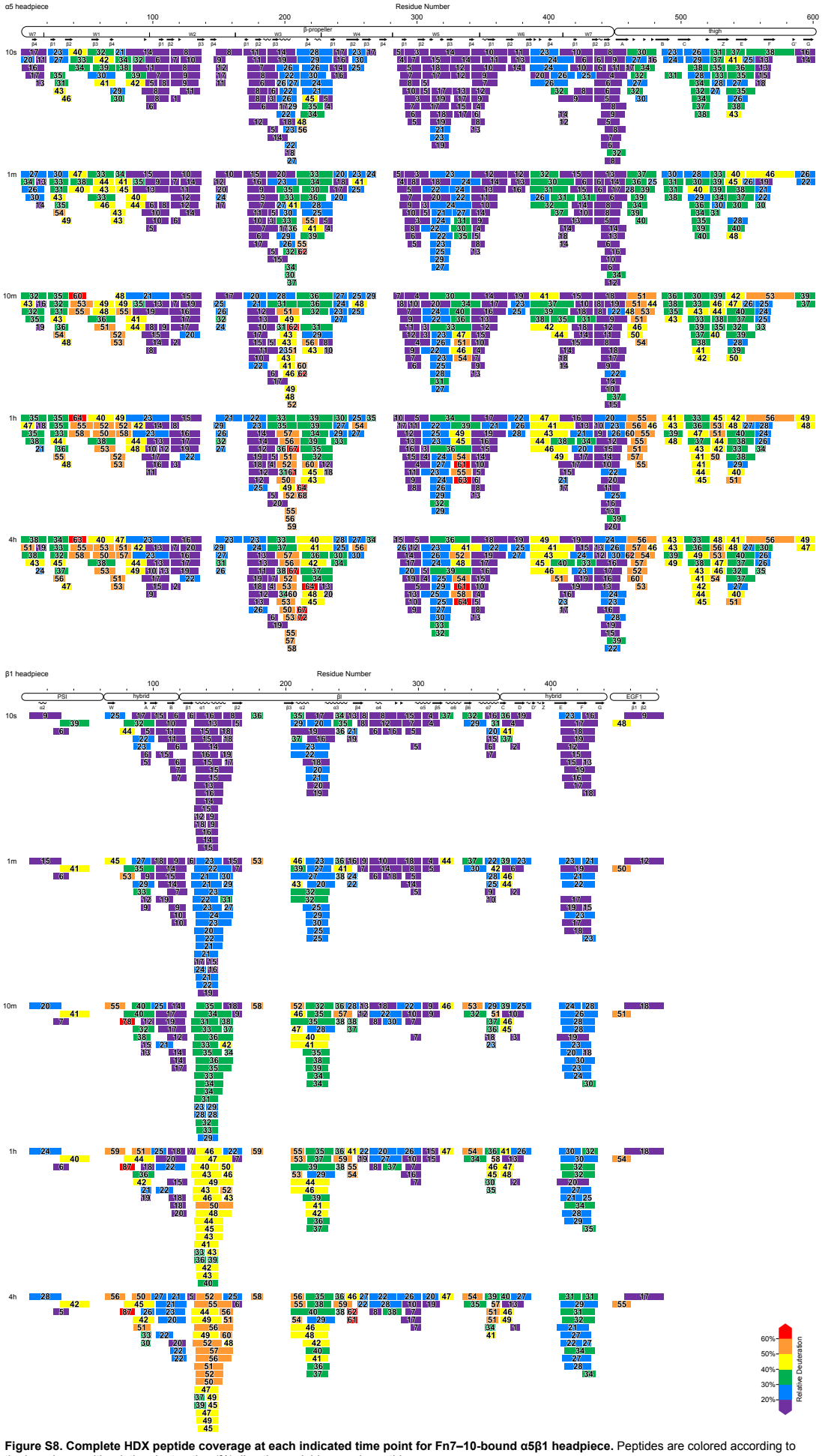

Figure S8. Complete HDX peptide coverage at each indicated time point for Fn7–10-bound α5β1 headpiece. Peptides are colored according to the key shown with relative deuteration (%) directly overlaid on each peptide.

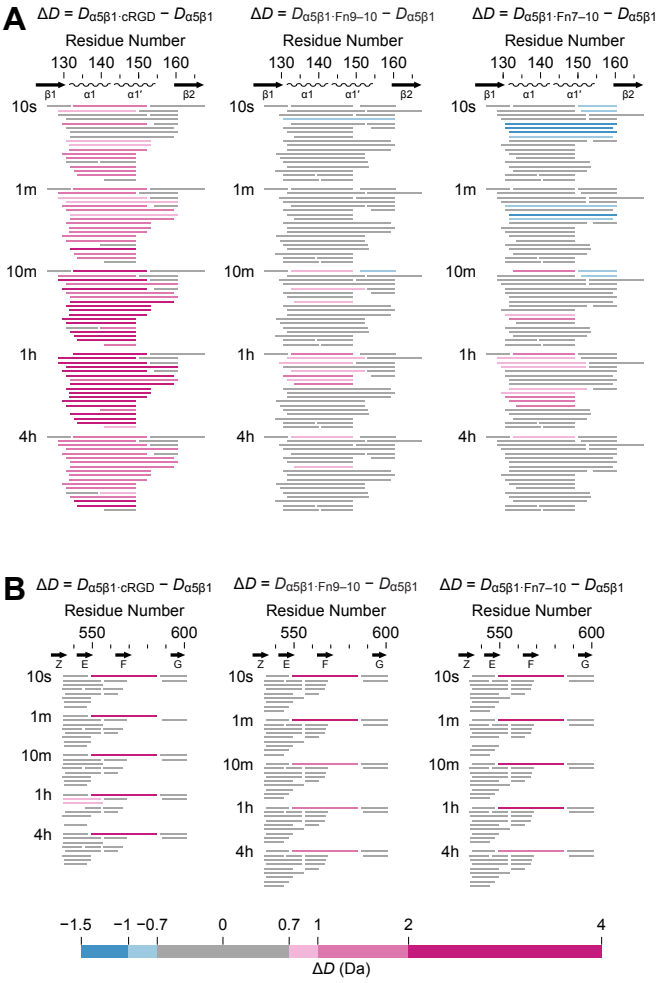

Figure S9. All overlapping peptides in the βI domain α1 and α1′ helices (A) and thigh domain F-G loop (B) region are shown on the sequence, with each row showing a different set of non-overlapping peptides. Each bar represents a peptide color coded according to its Δ*D*.